Elliptic flow of light nuclei in Au+Au collisions at $\sqrt{s_{NN}} = 14.5$ GeV

Master's Thesis

submitted to

Indian Institute of Science Education and Research Tirupati

in partial fulfillment of the requirements for the

BS-MS Dual Degree Programme

by

Abjasree S

Roll Number: 201501009

Supervisor: Dr. Chitrasen Jena

Department of Physics

Indian Institute of Science Education and Research (IISER) Tirupati

INDIA

March, 2020

Certificate

This is to certify that the MS Thesis entitled "Elliptic flow of light nuclei in Au+Au collisions at $\sqrt{s_{NN}} = 14.5$ GeV", submitted towards the partial fulfillment of the BS-MS dual degree programme at the Indian Institute of Science Education and Research Tirupati, represents the study / work carried out by Abjasree S at Indian Institute of Science Education and Research Tirupati under the supervision of Dr. Chitrasen Jena, Department of Physics, during the academic year 2019-2020 and the same has not been submitted for any other degree / diploma of any other university or institute.

Name of student: Abjasree S

Roll Number: 201501009

Signature of student:

Date : 31.03.2020

Name of Supervisor: Dr. Chitrasen Jena

Signature of Supervisor:
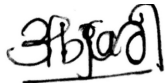
Date: 31/03/2020

Declaration

I declare that the matter presented in the MS thesis entitled "Elliptic flow of light nuclei in Au+Au collisions at $\sqrt{s_{NN}} = 14.5$ GeV", are the results of the work carried out by me at the Department of Physics, Indian Institute of Science Education and Research Tirupati, under the supervision of Dr. Chitrasen Jena. The contents are expressed in my own words and where others ideas have been included, I have adequately cited and referenced the original sources. I also declare that I have adhered to all principles of academic ethics and integrity and have not fabricated or falsified any idea / data / fact / image source in my submission.

I understand that violation of the above will lead to disciplinary action by the Institute and can also evoke penal action from the sources which have thus not been properly cited or from whom proper permission has not been obtained.

Name of student: Abjasree S

Roll Number: 201501009

Signature of student:

Date: 31.03.2020

Endorsed by:

Name of Supervisor: Dr. Chitrasen Jena

Signature of Supervisor:

Date: 31/03/2020

Acknowledgements

Abstract

The main goal of relativistic heavy-ion collision is to probe the state of matter at extreme temperature and energy density. The universe has undergone several phase transitions during its expansion, which marks as crucial epochs of the universe expanding after the big bang. During the phase transition at 10^{-11}s and temperature, T$\sim$100 GeV, the matter should have undergone an electroweak phase, and most of the fundamental particles are supposed to have acquired their Higgs masses. At 10^{-5}s and temperature, T$\sim$200 MeV, it should have undergone a strong-nuclear phase transition where hadronization took place. On the contrary to what we observe today, the matter and anti-matter should be in equal amount since they are produced during this phase transition. The relativistic heavy-ion collisions create a high dense-hot system that is similar to that of the early universe, which subsequently undergoes expansion and cooling, resulting in a range of temperatures and energy densities and perhaps different phases. After undergoing multiple interactions, eventually, the system gets thermalized, and Quark-Gluon Plasma (QGP) undertakes a collective expansion, which is accompanied by hadronization. The collective expansion that the system undergoes is known as flow. The flow is a crucial probe to know about the equation of state and the transport properties of the QGP.

The azimuthal anisotropy, v_2, is the explicit signature of collective flow in non-central heavy-ion collisions. In the relativistic heavy-ion collisions, the thermal production of light (anti-)nuclei may be difficult due to the small binding energy of the light (anti-)nuclei. So one expects that the light (anti-)nuclei to be formed in the later stage of evolution via coalescence of produced nucleons and antinucleons or participant nucleons. The coalescence probability is associated with the local nucleon density; hence production of light (anti-)nuclei is a vital probe to measure collective flow and freeze-out properties.

We present the study of transverse momentum and centrality dependence of the elliptic flow, v_2, of light nuclei in Au+Au collisions at $\sqrt{s_{NN}} = 14.5$ GeV. The Au+Au 14.5 GeV data ware taken using the STAR detector in the year 2014. The v_2 of light nuclei in Au+Au collisions at 14.5 GeV complements the previous measurements at STAR for other BES-I energies. The v_2 of the light nuclei are compared with its constituent nucleons to gain more insight about the coalescence mechanism. A model-based study of light nuclei elliptic flow is done using the AMPT model for better understanding of the light nuclei production.

Contents

List of Figures

List of Tables

Chapter 1

Introduction

1.1   The Standard Model of Elementary Particles

The quest to find the most fundamental particles from which the matter is made up of leads to the discovery of elementary particles. The discovery of elementary particles raised questions about their interactions, which lead to the study about their interactions. The theoretical predictions to predict the interactions were guided by the principles of the special theory of relativity and quantum mechanics and some other extra dividends. Then in the 1960s and 1970s, there emerged a theory that explained all the well known elementary particle interactions except gravity. This collection of related theories based on families of elementary particles is called *"Standard Model of the Elementary Particles"*. In the 1970s, a gauge theory emerged, describing the known elementary particle interactions except for gravity. This collection of related theories based on two families of elementary particles and incorporating quantum electrodynamics, the Glasgow-Weinberg-Salam theory of electro-weak processes and quantum chromodynamics constitute the standard model of elementary particles. According to this model, all the matter is made up of three kinds of elementary particles: leptons, quarks, and mediators. There are six leptons and are classified based on charge, electron number, muon number, and tau number. They fall into three generations, and there are also six anti-leptons with the sign reversed. The quarks are of six flavors based on the charge, strangeness, charm, beauty, and truth, and they also fall into three generations. For anti-quarks, all the signs are reversed. Moreover, all the quarks and anti-quarks comes in three colors, so there are 36 of them in total. Every interaction has its mediator. The interaction between individual quarks were studied to know about the strong force at its rudimentary level. The mediator which assist the quark interactions are *"gluons."* The standard model has 8 mediators. Gluons themselves carry color, so they do not exist as isolated particles,

and we detect them from other hadrons or colorless combinations of gluons called glueballs. The experimental evidence for the existence of gluons is from Deep inelastic scattering experiments in which half the momentum of the proton is carried by neutral constituents presumably gluons. So there are 12 leptons, 36 quarks, 12 mediators, and Glasgow-Weinberg-Salam theory calls for at least one Higgs particle, so a total of 61 elementary particles are there according to the standard model of elementary particle.

The coupling constant , which depends on the energy of the interaction, determines the strength of a force. If the coupling constant of the strong interaction is taken as 1, then for the electromagnetic interactions, it will be 10^{-3}, for weak interactions, it will be 10^{-16}, and for the gravity, it is 10^{-41}. As the energy increases, the coupling constants approach each other, and they may be equal at high energies. Then it might be possible to make a single formalism to all forces, and that is known as the grand unified theory. However, it is only possible at the energies of order 10^{19} eV.

1.2   Quantum Chromodynamics

Quantum Chromodynamics describes the strong interaction i.e., the interaction between the quarks and gluons in the standard model [1, 2]. It is similar to Quantum Electrodynamics for electrons. As electrons have the electric charge, quarks and gluons have the "color charge", hence the chromo component in theory. The coupling constant of the strong interaction, α_S, explains the two primary characteristics of QCD i.e., the confinement and asymptotic freedom. The coupling constant, α_S is given by

$$_S \approx \frac{12\pi}{(11n - 2f)ln(Q^2/\Lambda^2)} \tag{1.1}$$

where Q^2 is the momentum transfer, n is the number of colors, and f is the number of flavors. Λ denotes scale parameter and its value obtained from scattering experiments range from 100 MeV to 500 MeV as it's challenging to find the value of the Λ exactly from the experiments. The value of the $_S$ was determined by from various experiments and compared with perturbative QCD (pQCD) calculations as shown in Fig. 1.1 [3].

When there is only small momentum transfers or large distances, the $_S$ acquires a big value, and rapidly grows when the distance between two quarks are increased. For this reason, the quarks are never found free but can be found in a bound state of three as baryons or as the bound state of quarks and anti-quarks as mesons. This property of quarks is called the Confinement. But if the distance between the quarks is small,
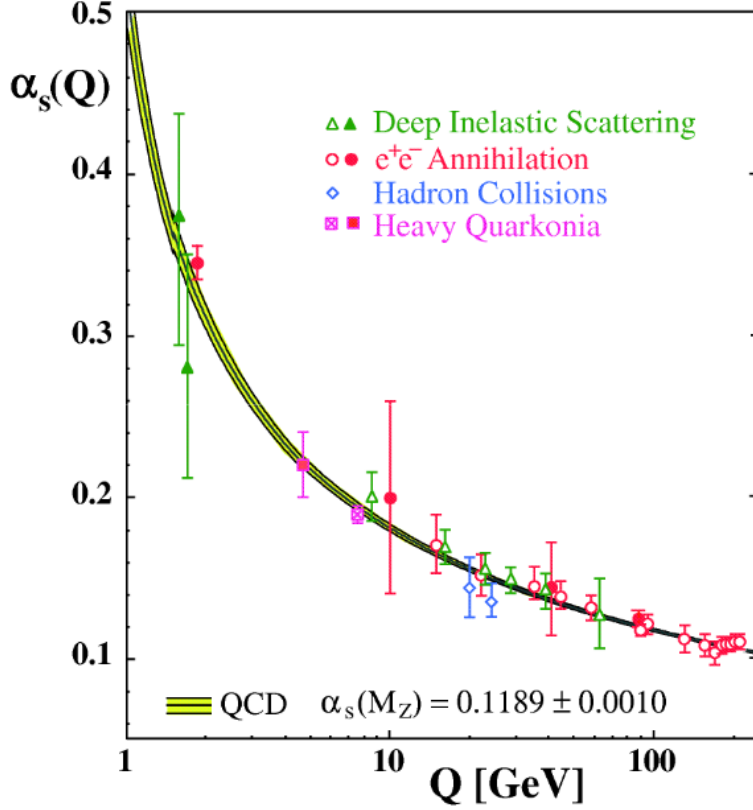
Figure 1.1: QCD prediction curves with the measurement of $_S$ from various experiments [3].

or the amount of the momentum transfer is high, the $_S$ will be small i.e., the coupling between the quarks will be less, so they behave as free particles. So at very high temperatures, the QCD medium is anticipated to be a gas of free quarks and gluons. This length scale, where the interactions between the quarks asymptotically goes to zero or becomes really weak, is known as Asymptotic Freedom. This property was discovered in 1973 by David Gross, Frank Wilczek, and David Politzer and received the Nobel Prize in 2004 for the same.

1.2.1 Deconfinement and Quark-Gluon Plasma

Soon after the discovery of the asymptotic freedom, Collins and Perry in 1975 suggested that the dense nuclear matter at the center of the neutron stars could be of free quarks and gluons [4]. The phase transition from a confined hadronic matter to the free quarks and gluons is predicted from the lattice QCD calculations at critical temperature $T_C \approx 170$ MeV and an energy density of $\epsilon \approx 1$ GeV/fm^3 [5, 6]. The state of matter consisting of free quarks and gluons is known as Quark-Gluon Plasma

(QGP). The QGP is a state of matter that is predicted to have existed in the first few microseconds of universe.

1.3 Relativistic Heavy-Ion Collisions

In 1974, T. D. Lee explained that a high dense state of nuclear matter with asymptotically free quarks is attainable by confining the high nucleon density in a relatively large volume. So the primary motivation for colliding the heavy ions at ultra-relativistic energies is the possibility to create a macroscopic volume of nuclear matter at extreme conditions. A phase transition from confined hadronic state to deconfined patronic state is predicted to happen under these very high temperature and energy density. Thus the first heavy-ion collisions were performed in the 1970s at modestly high energies at Lawrence Berkeley National Laboratory (LBNL). These initial experiments successfully motivated the study of the properties of compressed and exciting matter with the help of experiments at BNL (Brookhaven National Laboratory) and CERN (European Organization for Nuclear Research). The Relativistic Heavy Ion Collider (RHIC) at BNL is the first heavy ion collider in the world. It started operating from the year 2000 and has done collisions such as p+p, d+Au, Cu+Cu, Cu+Au, Au+Au, and U+U at the center of mass energies ranging from 7.7 GeV to 500 GeV. In 2010, the Large Hadron Collider(LHC) at CERN turned into the largest and powerful particle accelerator in the world when the lead nuclei collided at $\sqrt{s_{NN}} = 2.76$ TeV per nucleon pair. However, the top energy for p+p collisions in LHC is $\sqrt{s} = 13$ TeV.

1.3.1 Evolution of Heavy-Ion Collision

Two nuclei are accelerated in opposite directions with a velocity approximately equal to the speed of light in relativistic heavy-ion collisions. These nuclei, which travel with the relativistic speed is undergoes Lorentz contraction along the beam axis (i.e. z-axis), and it looks like pancakes as shown in Fig. 1.2. The impact parameter (b) characterizes the overlap region in the collision. The nucleons in the overlap region are called 'participants' and the nucleons outside the overlap region are called 'spectators'.

In the collision, the large amount of energy of the nucleus is deposited in the overlap region or interaction region of the both nuclei, which will lead to two possibilities. The one possibility is that the energy density of the nuclear matter will not reach the critical value for the formation of QGP, so it will evolve as the hadron gas as depicted in the left side of Fig. 1.3. The another possible outcome is the energy density will
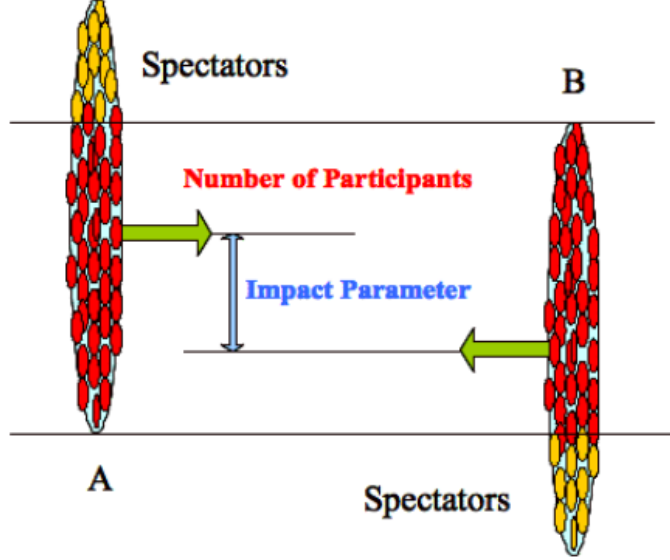
Figure 1.2: Collision of two nuclei with non-zero impact parameter showing the participant nucleons (red) and spectator nucleons(yellow) [11].

reach the critical values, and the QGP will be formed, as shown in the right side of Fig. 1.3. In order to reach the later stage, the initial density and temperature should be high enough i.e. the temperature should be above the critical temperature, T_C, then the phase transition occurs, and the quarks and gluons which were in the confined state will go to the deconfined state. That hot dense medium created in the heavy-ion collision is known as fireball. This fireball formed will not be in thermal equilibrium, but the subsequent interaction of quarks and gluons brings it into local thermal equilibrium at a proper time. This thermalized state of quarks and gluons is known as QGP. The relativistic hydrodynamics governs the further expansion of the system. The continues expansion and cooling of the system helps it to reach the critical temperature, T_C, and subsequently the hadronization starts. The quarks and gluons go to the confined state of hadrons as they continue to expand, and then they reach a temperature T_{ch}, where all the inelastic collisions between the hadrons stop so the relative abundance of the hadrons won't change anymore, and it is called the 'chemical freeze-out'. The expansion continues till the elastic interactions between the hadrons stop i.e., the mean free path of the hadrons will be larger compared to the size of the system, and this stage is called the 'thermal freeze-out' or 'kinetic freeze-out'. After this stage, the particles are detected by the detectors.
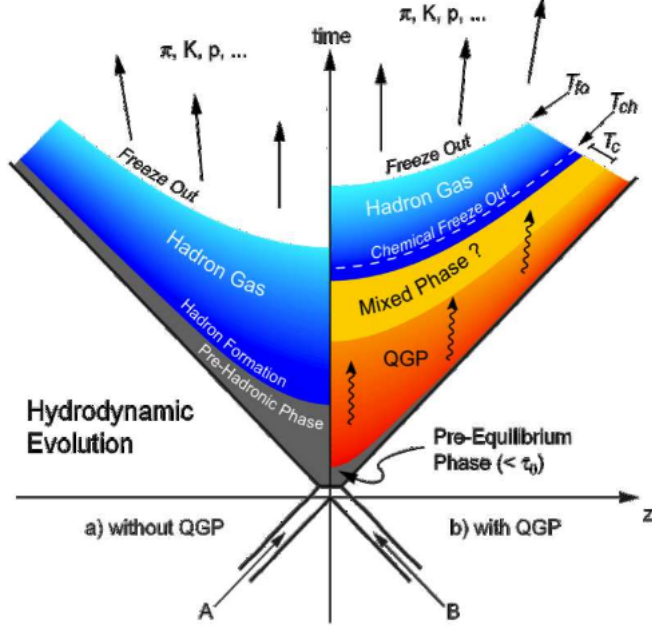
Figure 1.3: The space-time evolution of heavy-ion collision without QGP (left) and with QGP (right) in minkowski space [9].

1.4 Light (Anti-) Nuclei Production

The Big Bang theory describes the large scale evolution of our universe, and according to that, it should have created equal amounts of matter and anti-matter in the early universe [7, 8]. But as we observe today, all the things are made up of matter alone. So the mystery remains how the universe is full of matter even though we seldom find the anti-matter. The relativistic heavy-ion collisions produce an energy density same as that of early universe. So with the help of these experiments and by studying the subtle differences in the behavior of matter and anti-matter, we will gain more insight about this matter-antimatter asymmetry. The matter-antimatter symmetry is closely associated light nuclei and anti-nuclei production at high energies.

The high energy collisions create extreme energy densities and temperature, which creates the new state of matter i.e., QGP. The fireball produced in these collisions cools down to form the light nuclei such as d, t, ^3He, and their anti-particles in the final state. There are two possible mechanisms that explain the light nuclei and anti-nuclei production in heavy-ion collisions. The first mechanism is the thermal production of light nuclei-antinuclei pairs in which the thermal freeze-out plays an important role. But they seldom survive when the interactions between nucleons and other particles are strong, since the binding energy of light nuclei is small i.e.,

approximately equal to 2.2 MeV for d($\bar{d}$) and 7.7 MeV for the ^3He [12]. So the formation of light nuclei will only happen during the interaction among the nucleons and the other particles are really feeble i.e., at the later stage of evolution. The other mechanism for the light nuclei and anti nuclei production is by the recombination of created (anti-)nucleons or the stopped nucleons. This mechanism is known as the final state coalescence [31]. As we know, interactions between the particles will be weakening around the thermal freeze-out, so the study of light nuclei production helps to study the baryon distribution at that stage. This coalescence property is linked with the local nucleon density and characteristics of the hadronic system created in the final stage. In the coalescence model, the energy spectra of clusters are given by the product of the spectra of their constituent nucleons multiplied by the empirical coalescence factor [15, 16]. Therefore, studying the production of light (anti-)nuclei will provide information about the hadronization and the space-time evolution of the system. The integrated light nuclei yield can be compared with the other particle yields to get information about the chemical freeze-out properties using the statistical models.

The invariant yield of the nuclei is given as the function of the invariant yields of nucleons as given in Eq. 1.2

$$E_A \frac{d^3N_A}{d^3p_A} = B_A (E_p \frac{d^3N_p}{d^3p_p})^Z (E_n \frac{d^3N_n}{d^3p_n})^{A-Z} \approx B_A (E_p \frac{d^3N_p}{d^3p_p})^A, \qquad (1.2)$$

where N_A, N_p, and N_n denotes the yield of the nuclei and its constituent protons and neutrons, respectively. A is the mass number of the nuclei and Z is the atomic number of the nuclei. B_A is the coalescence parameter which is useful in the understanding the space-time geometry of the system [18]. The approximation is taken in the assumption that the neutrons and protons will have the identical momentum spectra. The coalescence parameter is related to the effective volume of the nuclear matter at the time of condensation of nucleons into nuclei which is called "nucleon condensation volume [17], "V_{eff}" which is given by

$$B_A \propto V_{eff}^{1-A} \qquad (1.3)$$

The production of the light nuclei will give more insight into the freeze-out parameters by comparing its yield with statistical models.

1.5 Elliptic flow of Light Nuclei

The overlap region of a non-central heavy-ion collision is spatially asymmetric like an almond shape, as depicted in Fig. 1.4. The pressure gradient due to the interactions
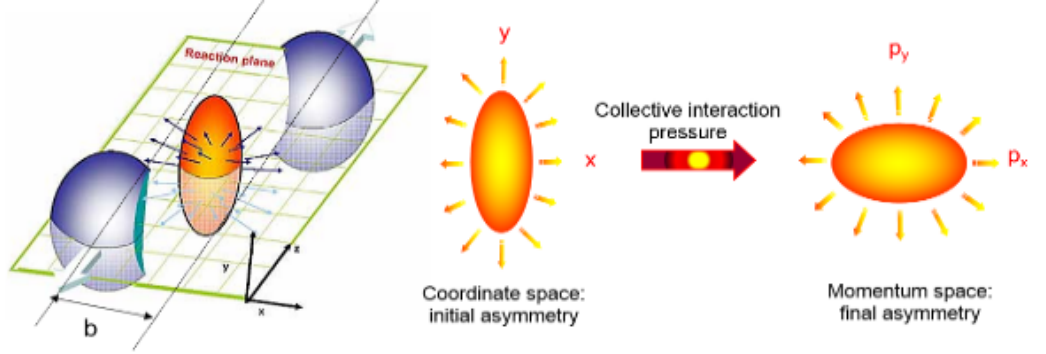
Figure 1.4: Schematic representation of initial spatial anisotropy changing itself into final momentum anisotropy [10].

will be larger among the short axis compared to the long axis of the almond-shaped collision region. The initial spatial anisotropy is transformed to the final momentum anisotropy, which is well pronounced in the azimuthal distribution of the produced particles. This azimuthal anisotropy is useful since it gives us the knowledge about the pressure at the early stage of heavy-ion collision [19].

The azimuthal anisotropy is quantified by expanding the azimuthal angle distribution of the produced particles with respect to reaction plane (the plane spanned by the beam direction and impact parameter vector) in a Fourier Series [21]:

$$E\frac{d^3N}{dp^3} = \frac{d^2N}{2\pi p_T dp_T dy}(1 + \sum_{n=1}^{\infty} 2v_n cos[n(\phi - \Psi_r)]), \tag{1.4}$$

where ϕ is the azimuthal angle of the particle, Ψ_r is the reaction plane angle, and v_n is the nth harmonic coefficient. The first harmonic Fourier coefficient v_1 is called the directed flow, and the second harmonic Fourier coefficient v_2 is called the elliptic flow. The elliptic flow of the identified particles in the heavy-ion collisions has been measured for a long time, and at low p_T (≤ 2 GeV/c) it is observed that the differential elliptic flow $v_2(p_T)$ for the hadrons scales with the particle mass of the hadrons [22]. The higher the hadron mass lower the value of v_2, which can be explained using the hydrodynamic calculations. The hydrodynamic calculations presume early thermalization and the ideal relativistic fluid expansion, which played an important role in the evolution of QGP medium. For $p_T \geq 2GeV$, the hydrodynamic calculations seems to over estimate the data. When the v_2 values are divided with the constituent quarks (i.e., n=2 for mesons and n=3 for baryons), we observe a scaling pattern for all hadrons, known as the Number of Constituent Quark (NCQ) scaling. The NCQ

scaling depicts that at the intermediate p_T range ($0.6 \leq p_T/n \leq 2$ GeV/c), the v_2 of the identified hadrons scales with the number of constituent quarks. This NCQ scaling is important because it provides us the information that the quarks and gluons will be in their deconfined state. The high energy nuclear collisions help to prove that the hadrons are produced via coalescence of the constituent quarks. In the quark coalescence model, two nearest quark and anti-quark are combined into mesons, and three nearest quarks or anti-quarks are combined into baryons or antibaryons, but the patrons are not directly observed from the experiment, so it's difficult to understand the local correlations in quark coalescence. The light nuclei and anti-nuclei production happen through final state coalescence at the time of thermal freeze-out. So the NCQ scaling can be used to predict the v_2 of light nuclei, which follows atomic mass number ordering [17]. In the case of nulcleon coalescence, both the nuclei and its constituents are directly observed from the experiments. So we can study the v_2 of the nuclei and its constituents and compare them, which helps to give more insight about the freeze-out dynamics and the coalescence mechanism.

Chapter 2

The STAR Experimental Setup

2.1 Relativistic Heavy Ion Collider (RHIC)
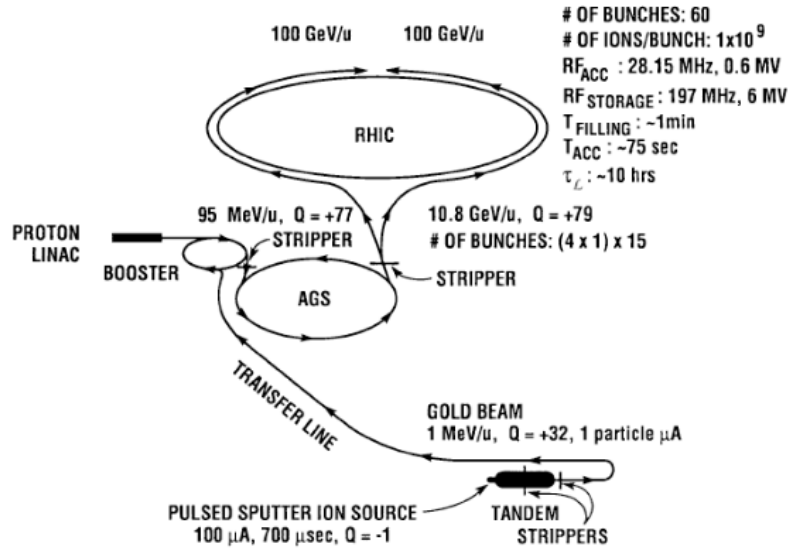
Figure 2.1: The schematic diagram showing the different acceleration stages of ions at RHIC [25].

The Relativistic Heavy Ion Collider at Brookhaven National Laboratory (BNL) is the first heavy ion collider that is efficient enough to collide various heavy ions at relativistic energies [28]. The construction of RHIC was completed in the year, 1999 and the first data takking run was in the year 2000 by colliding Au+Au beams. The RHIC is constructed mainly for colliding the heavy ions but subsequently it was used for the spin physics program by colliding the polarized protons. The schematic

diagram of the RHIC accelerator is shown in Fig. 2.1. The schematic diagram exemplifies the different stages of the acceleration of ions at RHIC.

Another important feature of RHIC is that it can measure the processes with a small cross-section since it provides the beams with high luminosities. The event rate R_i for a process with cross-section σ_i is given by

$$R_i = \sigma_i L \tag{2.1}$$

where L is the Luminosity which is given by

$$L = fn\frac{N_1 N_2}{A} \tag{2.2}$$

where f is the frequency of the revolution, n is the number of bunches per beam, A is the cross-sectional area of overlap between the colliding beam of particles, and N_1 and N_2 are the number of particles contained in each bunch. Therefore, it can reach high luminosities by increasing f, n, and reducing the beam profile.
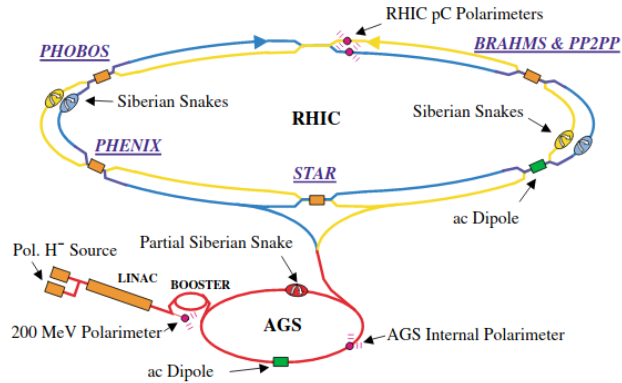
Figure 2.2: RHIC accelerators in BNL, New York [26]

There are six interaction points in the RHIC rings, and there are four experiments that are located in the four interaction points. They are Solenoidal Tracker at RHIC (STAR) [29], Pioneering High Energy Nuclear Interaction Experiment (PHENIX) [30], Broad Range Hadron Magnetic Spectrometer (BRAHMS) [31] and PHOBOS. BRAHMS and PHOBOS [32] were two small experiments, they finished the data taking during the year 2005 to 2006. The two major experiments STAR and PHENIX were continuing its data taking till the year 2016 when PHENIX completed its data taking. Currently, only STAR experiment is taking data at RHIC.
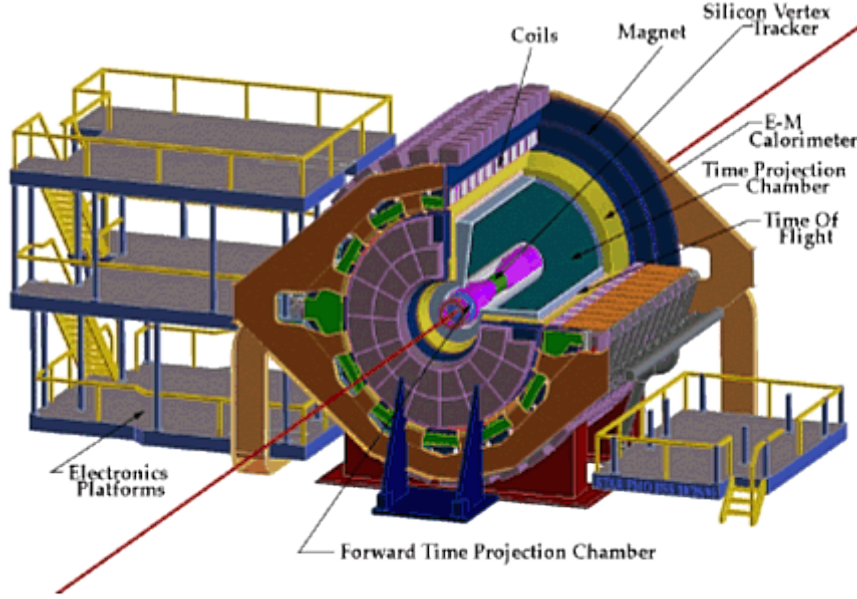
Figure 2.3: The schematic diagram showing the different components of the STAR detector [27].

2.2   The STAR Detector at RHIC

The STAR detector is one of the major detectors in the RHIC [29]. The ultimate goal of the STAR experiment is to get the fundamental understanding of the hadronic interactions and get more insight into the new state of matter i.e., QGP. The STAR experiment was designed with different sub-detectors that are capable of detecting different particles and their trajectories. To study the phase transition and space-time evolution of ultra-relativistic collisions, we measure many observables simultaneously. STAR has an excellent detector system for high precision tracking, momentum measurement, and particle identification at the central rapidity region [29]. The steady magnetic field of 0.5 T aligned in the direction of beam using the solenoidal magnet of the STAR detector helps in the momentum measurements of different charged particles. The charged particle tracking and particle identification are done by the Time Projection Chamber (TPC) [33], which is at the center of the STAR detector. It is a 4.2 m long detector which identifies particles within $|\eta| \leq 1.8$ with full azimuthal coverage. For the extension of tracking in both forward and backward direction, two Forward Time Projection Chamber (FTPC) [34] detectors were installed in the pseudorapidity range from $2.5 \leq \eta \leq 4.0$ and it covers the full XY plane azimuthally. In order to do the particle identification in larger momenta for a small solid angle, a barrel Time of Flight (TOF) detector which works in the principle of

Multi-gap Resistive Plate Chamber (MRPC) [35] was installed in STAR experiment in the year 2010. The TOF has 120 trays, which measure pseudorapidity $|\eta| \leq 0.9$ within full azimuthal coverage. The Calorimeters were framed for the detection of the electromagnetic particles in STAR. They find the transverse energy placed by the electrons and photons. The Endcap Electromagnetic Calorimeter (EEMC) [37]covers the pseudorapidity range $1 \leq \eta \leq 2$ and the full Barrel Electromagnetic Calorimeter (BEMC) [36] covers the pseudorapidity range $|\eta| \leq 1.0$. The energy placed by the single photons or photon pairs produced by either from the neutral pion (π^0) otherwise from the η meson decay is differentiated by Shower Maximum Detectors (SMD). The event triggering is done with the help of two Zero Degree Calorimeters (ZDCs), two Beam-Beam Counters (BBCs), and two upgraded Pseudo Vertex Position Detectors (VPDs). The Photon Multiplicity Detector (PMD) [38], which covers a pseudorapidity range of $-3.7 \leq \eta \leq -2.3$, is for detecting photons at forward rapidity with full azimuthal coverage.

2.2.1   Trigger Detectors

The STAR detector detects both charged and neutral particles produced in the heavy-ion collisions. The trigger system plays an important role in deciding which events should be considered for data recording at all beam crossings. The STAR data is nimble and versatile enough to record data from various detectors at a broad range of readout rates. For beams with high luminosities, the interaction range reaches ~ 100 MHz. However, the major part of the data is from TPC, FTPC, and EMC, which are slow detectors operating ~ 100 Hz, so all events are not recorded by DAQ. So, we use STAR trigger system to select events in the slow detectors by using the input from the fast detector to record data. The events with exceptional or distinct signals for consideration can also be selected to enlarge the recorded statistics using the trigger system. The two ZDCs, two BBCs, and two VPDs are the central trigger systems in STAR.

2.2.2   Time Projection Chamber (TPC)

The TPC is the primary tracking subsystem in the STAR detector, which covers a pseudorapidity range of $|\eta| < 1.8$ with complete azimuthal coverage [33, 39]. TPC identifies the charged particles by tracking by its ionization energy loss. It identifies the charged particles over the momentum range from 100 MeV/c to greater than 1 GeV/c. It can measures the momenta of charged particles from 100 MeV/c to 30 GeV/c.

TPC technical design
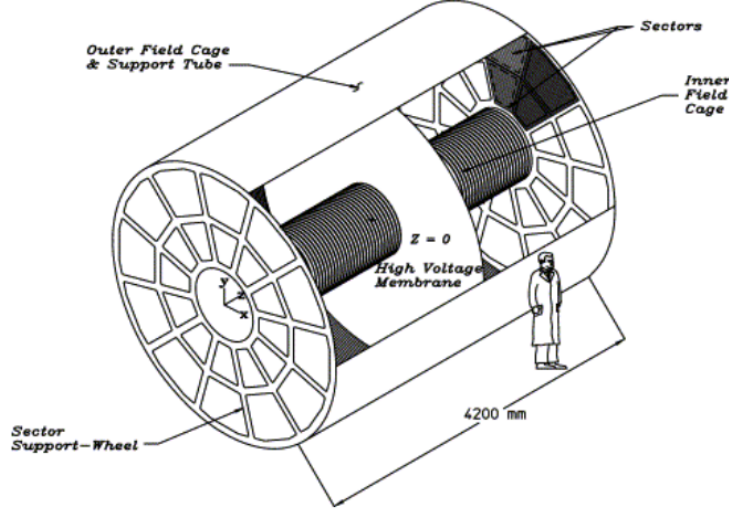
Figure 2.4: The schematic diagram of TPC showing its different parts [33].

The TPC is a long cylinder of length 4.2 m and the external diameter 4 m, as shown in Fig. 2.4. It is within the solenoidal magnet which produces a steady magnetic field 0.5 T along the direction of beam. The charged particles to bend from the collision point while passing through the detector because of the magnetic field. It has one outer field cage (OFC), one inner field cage (IFC), and two end caps as depicted in the Fig. 2.4. The OFC and IFC provide an ideal electric field for the electrons to drift to the anode plane. It also helps to preserve the TPC gas without contamination from the outside air. The end caps are like anode as it provides the ground potential for the readout system.

TPC is filled with P10 gas i.e. 90 percent argon added with 10 percent methane, which is maintained at 2 mbar above the normal atmospheric pressure. This particular gas is chosen due to its fast drift velocity at the low electric field which helps to make the drift velocity steady and constant even though there is small fluctuations in temperature and pressure. The detector design is made simple since lower field strength requires a lower voltage. The electron drift velocity in P10 is really fast, 5.45 $cm/\mu s$ at 130 V/cm drift field. The TPC readout system is the Multi-Wire Proportional Chamber (MWPC), which is situated at the endcaps.

Track Reconstruction in TPC

The first step for track reconstruction is to identify the 3-D space coordinate points (x,y,z) of the charged particles. The charged particles ionize the gas atoms and

molecules in its way when it passes through the TPC. Due to the large electric field between the central membrane and the anode plane, these ionized electrons move towards the anode in a straight path since the axial magnetic field of the STAR magnet restricts its motion. The signal obtained from the adjacent pads gives information about the xy position when the electron reaches the anode plane. The z-position of cluster is obtained by multiplying the drift time obtained from the origin of cluster in the anode with the average drift velocity. As we obtain (x,y,z) positions, we reconstruct the tracks with the helical trajectory fit implemented in the Time Projection Chamber (TPC) algorithm. But there will be a deviation from the helical shape due to energy lost by the particles and the multiple scattering it did even though each track is a helix of the first order.

The global track is found by collecting more tracking details from the inner detectors and by refitting it with Kalman Fit Method [40]. The reconstructed global tracks are extrapolated back to origin to find the z-position of primary collision vertex. The track reconstruction to incorporates the primary vertex to be a extra space point if the distance of closest approach (DCA) (to primary vertex) is less than 3 cm, and they are called primary tracks. The track quality cuts, particle types, and track multiplicity determine track reconstruction efficiency in TPC.

Particle Identification using TPC

The energy loss (dE/dx) of charged particles due to their interaction with the gas inside the TPC is used to identify them. A maximum of dE/dx points on all 45 pad rows are obtained if the particle passes through the entire volume. It is not possible to obtain a precise value for average dE/dx due to huge ionization fluctuations, but the particle loses it's energy in a small length, so the most probable dE/dx is used instead. This dE/dx value is computed by deleting the 30 percent highest ionization clusters and finding the truncated mean of clusters which are left.

The ionization energy loss can be calculated from the Bichsel function [41] which is an extension of Bethe-Bloch formula [42] for a given track momentum and particle mass which is given by :

$$-\frac{dE}{dx} = Kz^2\frac{Z}{A}\frac{1}{\beta^2}[\frac{1}{2}ln(\frac{2m_ec^2\beta^2\gamma^2T_{max}}{I}) - \beta^2 - \frac{\delta^2}{2}], \tag{2.3}$$

where K is a constant, z is the integral charge of the particle, Z is the atomic number of the absorber, A is the atomic mass of the absorber, m_e is the mass of electron, c is speed of light in vacuum, I is the average ionization energy of material, T_{max} is the maximum kinetic energy given to a free electron in an interaction, δ is the energy density correction, and $\beta\gamma$ = p/mc, where p and m are momentum and mass

of the charged particle, respectively. So, this is a mass-dependent equation of dE/dx hence is useful for particle identification. The dE/dx resolution in TPC is around 7-8 percent. The pions and kaons are identified up to transverse momentum 0.75 GeV/c and the protons and antiprotons up to 1.1 GeV/c.

The standard deviation of a Gaussian between the measured track and expected value gives the quantitative description of particle identification by the variable $n\sigma$ given by

$$n\sigma_X = \frac{1}{R} log \frac{< dE/dx > |_{measured}}{< dE/dx >_X |_{expected}} \tag{2.4}$$

where X is the particle type (e, π, K or p), and $< dE/dx > |_{measured}$ is the experimental energy loss of the track and $< dE/dx >_X |_{expected}$ is the theoritical energy loss. The Z is another variable used for particle identification given by

$$Z_i = ln(\frac{< dE/dx > |_{measured}}{< dE/dx >_i |_{expected}} \tag{2.5}$$

where $< dE/dx > |_{measured}$ is the experimental mean energy loss of the track and $< dE/dx >_i |_{expected}$ is the theoretical mean energy loss calculated using Bischsel function for the given particle type (i = d,t and ^3He).

2.2.3 Time Of Flight (TOF)
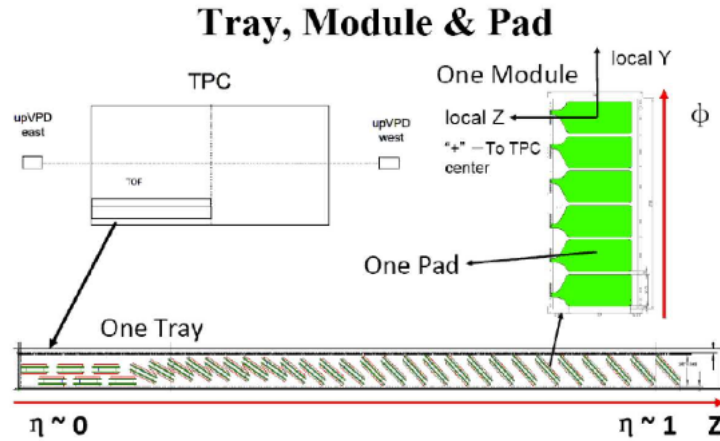
Figure 2.5: The geometry of each pad in TOF subsystem [11].

$$m = p/(\beta\gamma c) \tag{2.6}$$

where $\gamma = 1/\sqrt{1 - \beta^2}$. So these can been used for the particle identification process.

Chapter 3

Data Analysis

3.1 Elliptic Flow

The 'flow' in the heavy-ion collisions means the collective motion of particles produced in the process due to high pressure arising from the compression and heating of nuclear matter. This flow is divided into two categories based on their expansion i.e.

1. Longitudinal flow: expansion along the beam direction

2. Transverse flow: expansion along the transverse plane

The transverse flow can again be divided into two i.e., Radial flow and Anisotropic flow. Radial flow is the expansion of particles isotropically due to pressure gradients, whereas the Anisotropic flow is the expansion, which is due to the anisotropy in pressure. We intend to work on the anisotropic flow of light nuclei in the Au+Au collisions.

The system created in the head-on heavy-ion collision is different from that of the peripheral collision since the heavy-ions are extended objects. In order to study the properties of the system, they are divided into different centrality groups, which are presented later in this thesis. The transverse distance between the centers of two colliding ions is the impact parameter (b). The overlap region, particle production, and interactions are more in central collisions, whereas the spatial anisotropy of the overlap region is more in peripheral collisions [20]. So the initial spatial anisotropy with respect to the x-z plane (reaction plane) will be transferred to momentum anisotropy of the produced particles due to the pressure gradient developed by the constituents. These anisotropies are quantified using the flow harmonics v_n.

Flow harmonics, v_n, is used for the experimental measurement of anisotropies. The invariant yield of the particles produced can be expanded in the form of Fourier

series [21]:

$$E\frac{d^3N}{dp^3} = \frac{d^2N}{2\pi p_T dp_T dy}(1 + \sum_{n=1}^{\infty} 2v_n cos[n(\phi - \Psi_r)]) \qquad (3.1)$$

where ϕ is the azimuthal angle of the particle, Ψ_r is the reaction plane angle and v_n is the nth harmonic coefficient. The nth order Fourier coefficient v_n is given by [43]:

$$v_n = < cos[n(\phi - \Psi_r)] > \qquad (3.2)$$

where the average is taken over all particles in all events. The first coefficient v_1 is called the directed flow, and the second coefficient v_2 is called the elliptic flow. The v_2 is called the elliptic flow because in the polar coordinates for the small values of v_2, the azimuthal distribution with non-zero second harmonic describes an ellipse. Here we are interested in the elliptic flow given by:

$$v_2 = < cos[2(\phi - \Psi_r)] > \qquad (3.3)$$

For the estimation of v_2 for the light nuclei we use event plane method.

3.2 Data Set used and Analysis Procedure

We worked on the data set collected for Au+Au collisions at $\sqrt{s_{NN}} = 14.5$ GeV using the STAR detector at RHIC in the year 2014. This data set was obtained with minimum bias trigger. The minimum bias trigger needs the coincidence of the two ZDCs, which are located $\pm$ 18 m from the center of the interaction region along the beam line.

3.2.1 Event Selection Criteria

The primary vertex is obtained by extracting the best point which describes the common emergence of tracks from TPC. The events should have position of primary vertex along z-direction, V_z, within $\pm$ 70 cm from the center of TPC. This is to ensure uniform acceptance in the η range, because the events far away from the interaction point will cause a loss in acceptance. The event vertex radius, V_r ($= \sqrt{V_x^2 + V_y^2}$), should be less than 1 cm for rejecting the events involving beam-pipe and beam-gas interactions. The various event quality cuts used for this analysis are listed in Table 3.1. The basic QA plots for the events are shown in Fig. 3.1. The number of events available for the analysis after applying these cuts is 18 M.
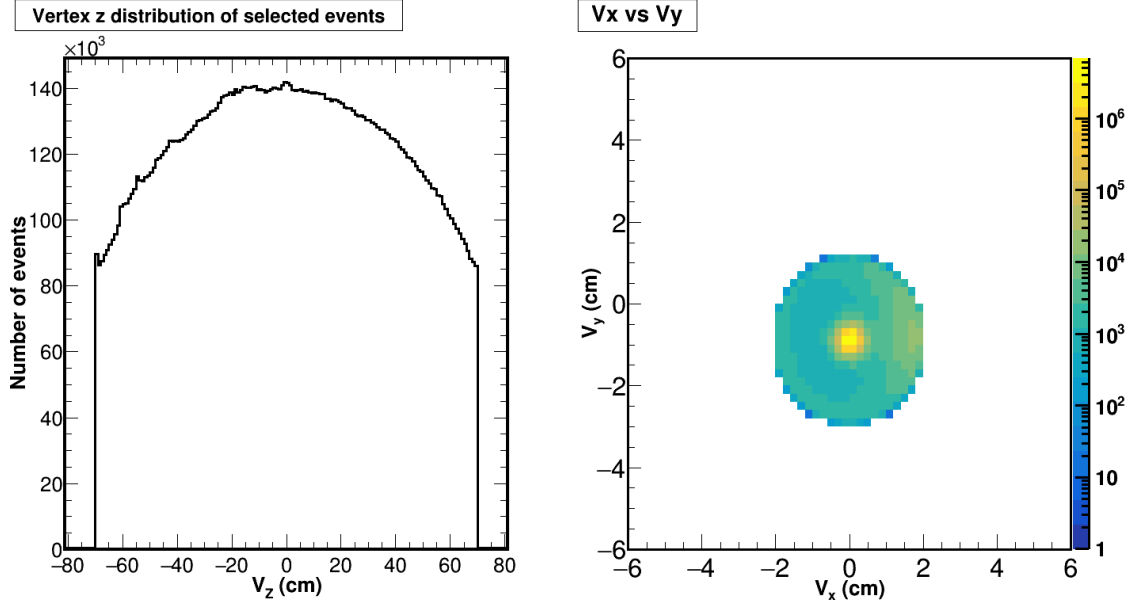
Figure 3.1: Event-by-event distribution of z-position (V_z) as well as the x-y position $(V_y$ vs. $V_x)$ of the primary vertex in Au+Au collisions at $\sqrt{s_{NN}} = 14.5$ GeV.

Table 3.1: Event selection criteria for light nuclei study in Au+Au collisions at $\sqrt{s_{NN}}$ = 14.5 GeV.

variable	condition
V_z	-70 < V_z < 70 cm
V_r	0 < V_r < 2 cm

3.2.2 Track Selection Criteria

In this analysis, several track quality cuts are applied to all tracks of TPC to select the good quality tracks. The distance of closest approach (DCA) between each track and event vertex is kept to be lower than 3 cm in order to avoid the admixture of tracks from the secondary vertex. A minimum of 25 fit points is used in reconstructing each track in order to avoid the multiple counting of split tracks. The tracks can at most have 45 hit points in TPC. In order to confirm that the tracks have quality $< dE/dx >$ values, the fit points for (dE/dx) i.e. nHitsdEdx is kept to be ≥ 15. The low p_T tracks, i.e. $p_T < 0.1$ GeV/c, is avoided since they have large curvature inside the solenoidal magnetic field, so they cannot traverse the entire TPC. The various track quality cuts used for this analysis are listed in Table 3.2. The basic QA plots for the track variables are shown in Fig. 3.2 and 3.3.
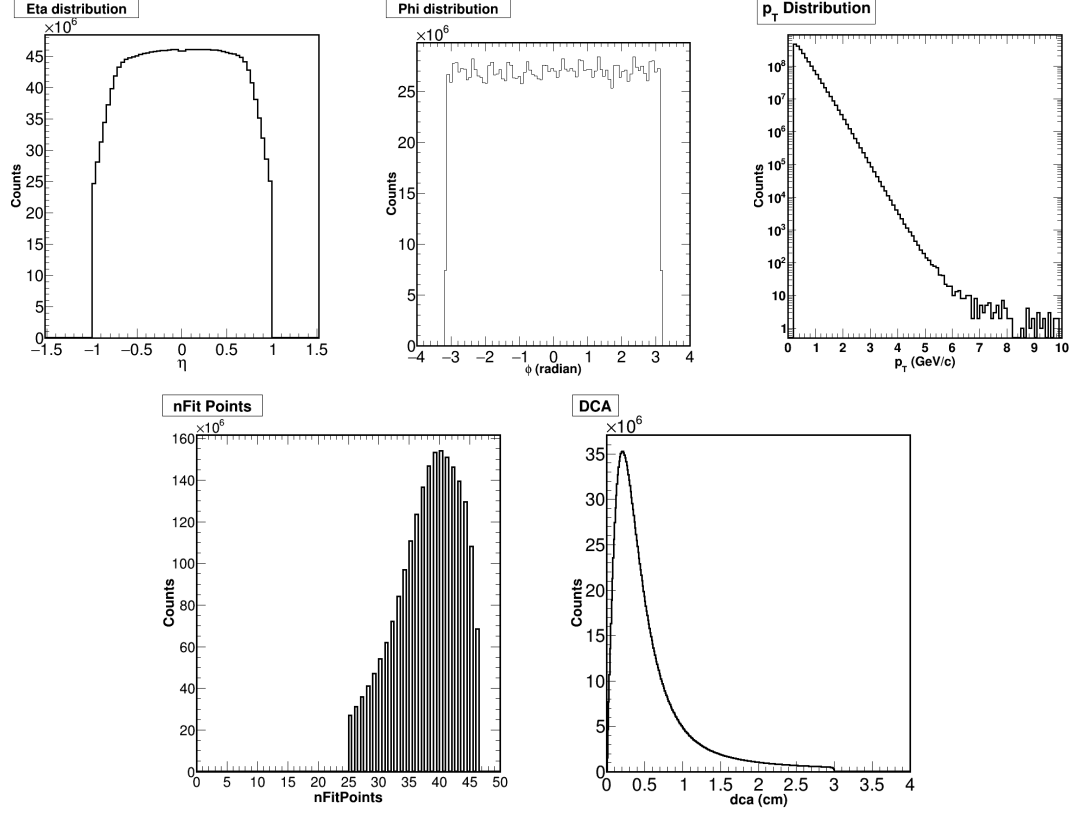
Figure 3.2: The distributions of track variables (η, ϕ, p_T, nHitsFit and DCA) in Au+Au collisions at $\sqrt{s_{NN}} = 14.5$ GeV.

Table 3.2: Track selection criteria for light nuclei study in Au+Au collisions at $\sqrt{s_{NN}}$ = 14.5 GeV.

variable	condition
Number of fit points (nHitsFit)	≥ 25
Fit points for (dE/dx) (nHitsdEdx)	≥ 15
nHitsFit / nHitsPos	≥ 0.52
Distance from primary vertex (DCA)	≤ 3.0 cm
Transverse momentum (p_T)	≥ 0.1 GeV/c
pseudorapidity ($|\eta|$)	≤ 0.5
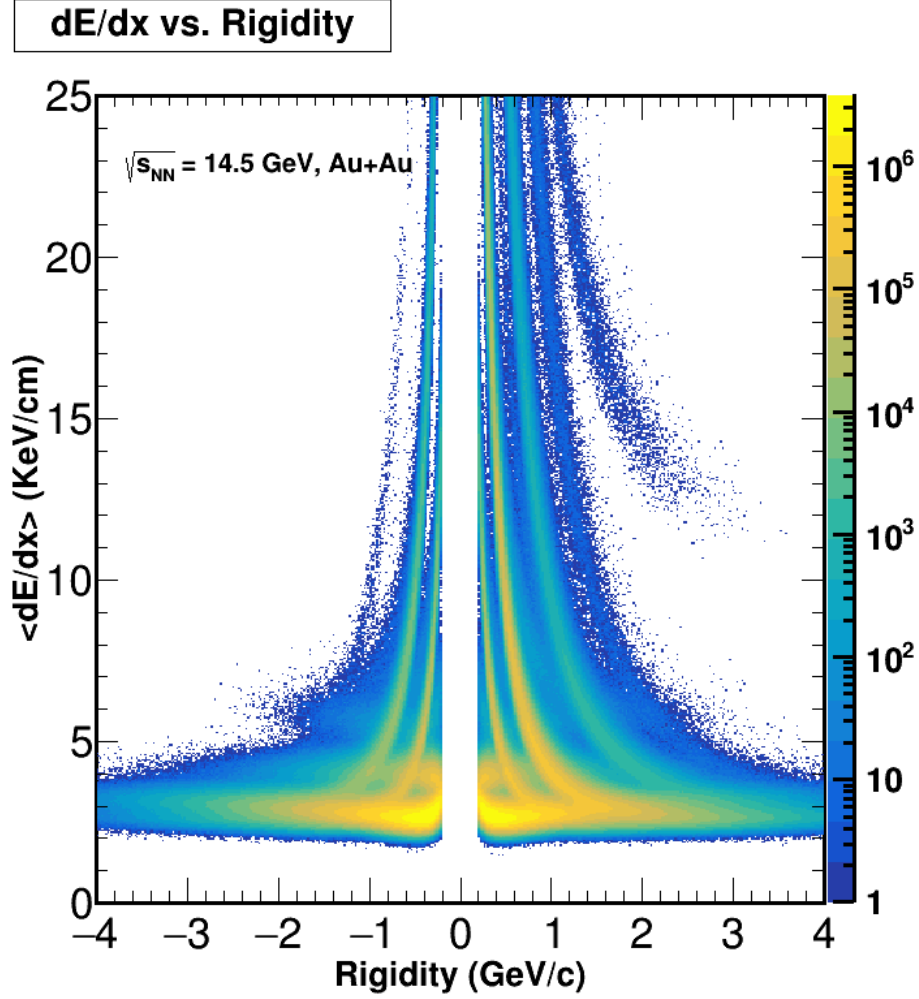
Figure 3.3: The dE/dx as a function of rigidity obtained from TPC in Au+Au collisions at $\sqrt{s_{NN}} = 14.5$ GeV.

3.2.3 Centrality Selection

The centrality of Au+Au collisions is defined by using the uncorrected charged-particle multiplicity distribution reconstructed in the main TPC over the full azimuth and pseudorapidity range $|\eta| < 0.5$. Figure 3.4 shows the uncorrected charged-particle multiplicity distribution for Au+Au collisions at $\sqrt{s_{NN}} = 14.5$ GeV. The charged-particle distribution is fitted with multiplicity distribution from the Glauber Monte-Carlo simulations to determine the event centrality. The simulated multiplicity distribution is calculated from a two-component model given by

$$\frac{dN_{ch}}{d\eta}|_{\eta=0} = n_{pp}\left[(1-x)\frac{N_{part}}{2} + xN_{coll}\right],\tag{3.4}$$
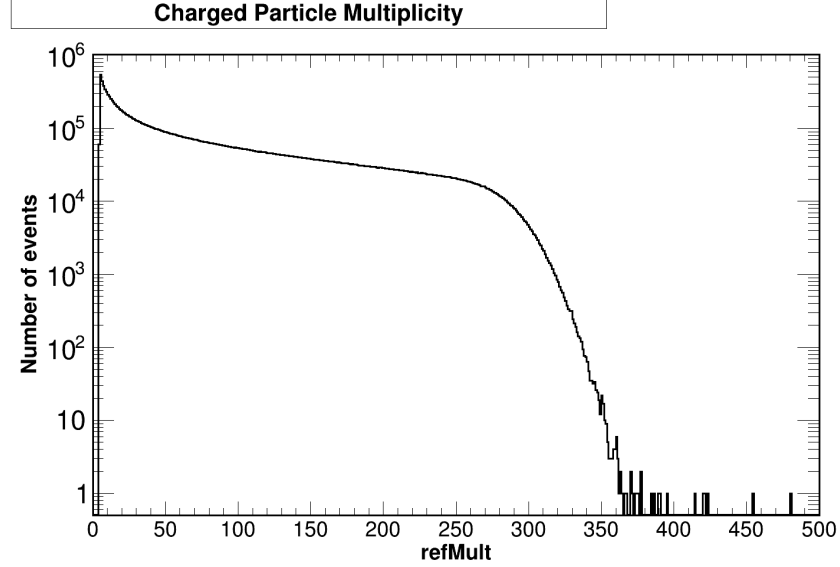
Figure 3.4: The uncorrected charged-particle multiplicity distribution in Au+Au collisions at $\sqrt{s_{NN}} = 14.5$ GeV.

where the N_{part} is the number of participant nucleons and N_{coll} is the number of binary collisions.

3.2.4 Particle Identification Method

The main TPC of STAR experiment was used to identify the particles in the 2014 run. The energy loss (dE/dx) of charged particles due to their interaction with the gas inside the TPC is used to identify them. Figure 3.3 depicts the dE/dx of charged tracks as a function of rigidity. The theoretical ionization energy loss can be calculated from the Bichsel function, which is an extension of Bethe-Bloch formula for a given track momentum and particle mass which is given by :

$$-\frac{dE}{dx} = Kz^2\frac{Z}{A}\frac{1}{\beta^2}[\frac{1}{2}ln(\frac{2m_ec^2\beta^2\gamma^2T_{max}}{I}) - \beta^2 - \frac{\delta^2}{2}] \tag{3.5}$$

where K is a constant, z is the integral charge of the particle, Z is the atomic number of the absorber, A is the atomic mass of the absorber, m_e is the mass of electron, c is speed of light in vacuum, I is the average ionization energy of material, T_{max} is the maximum kinetic energy given to a free electron in an interaction, δ is the energy density based correction, and $\beta\gamma = $ p/mc, where p and m are momentum and mass of the charged particle, respectively. The Z is a variable used for the quantitative description of particle identification which is given by

$$Z_i = ln(\frac{< dE/dx > |_{measured}}{< dE/dx >_i |_{expected}}) \tag{3.6}$$

where $< dE/dx > |_{measured}$ is the experimental mean energy loss of the track and $< dE/dx >_i |_{expected}$ is the theoretical mean energy loss calculated using Bischsel function for the given particle type (i = d and ^3He). Figure 3.5 shows the Z-distribution of d and ^3He for different p_T bins in Au+Au collisions at $\sqrt{s_{NN}} = 14.5$ GeV. The raw yields are extracted by fitting these distributions with double Gaussian function.
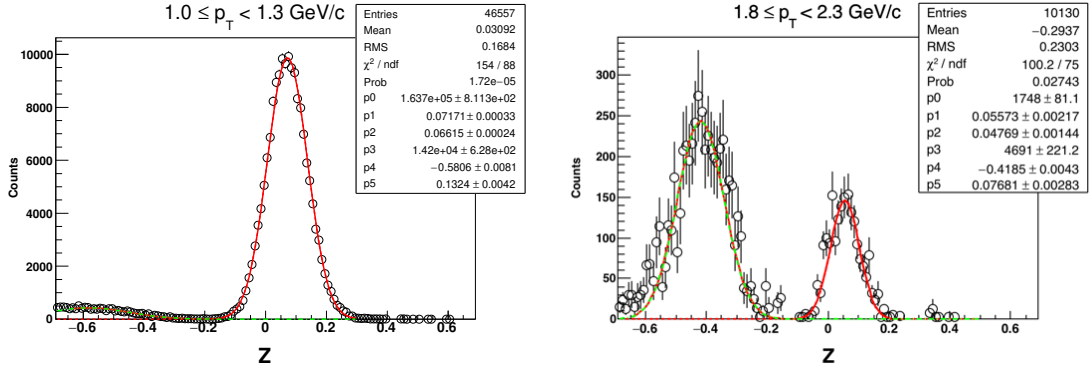
Figure 3.5: Z distributions of d (left panel) and ^3He (right panel) for $0 < \phi - \Psi_2 < \pi/10$ in Au+Au collisions at $\sqrt{s_{NN}} = 14.5$ GeV. The Z distributions for each species is fit with a two-Gaussian function. One Gaussian is used to describe the Z distribution for the nuclei of interest (red dashed line) and another Gaussian is used to describe the background (green dot-dashed line).

3.2.5 Event Plane Estimation and v_2 measurement

In the experiment, we cannot obtain the impact parameter between two nuclei and so it's not possible to directly measure the reaction plane. The reaction plane can be estimated on an event-by-event basis from the azimuthal particle distribution. The reaction plane estimated this way is known as Event Plane. The event plane angle is obtained from the flow vector Q_n whose components are given by:

$$X_n = Q_n cos(n\Psi_n) = \sum_{i=1}^{N} \omega_i cos(n\phi_i) \tag{3.7}$$

$$Y_n = Q_n sin(n\Psi_n) = \sum_{i=1}^{N} \omega_i sin(n\phi_i) \tag{3.8}$$

where ω_i is the weight and N is the total number of produced particles in the given acceptance used for the flow vector calculation in an event. The p_T of the particle is taken as the weight factor for this analysis. The n_{th} harmonic event plane is given by

:

$$\Psi_n = \frac{1}{n}tan^{-1}\left(\frac{\sum_{i=1}^{N}\omega_i sin(n\phi_i)}{\sum_{i=1}^{N}\omega_i cos(n\phi_i)}\right) = \frac{1}{n}tan^{-1}\left(\frac{Y_n}{X_n}\right) \tag{3.9}$$

The event plane angle Ψ_n determined will be in the range $0 \leq \Psi_n \leq 2\pi/\text{n}$.

3.2.6 Event Plane Acceptance Correction

The finite acceptance of the detectors will cause the particles to be azimuthally anisotropic in the laboratory frame, which makes bias in the measurement, and the azimuthal distribution will not be flat. So, we need to make the event plane distribution isotropic in the laboratory. The two methods used to remove the effects of anisotropy are:

1. **Recenter Correction**: In this method we recenter the distribution of flow vectors (Q_X, Q_Y) by subtracting the flow vector values averaged over all events ($< Q_X >$, $< Q_Y >$) . However, this method won't remove higher order harmonics which is present in the resulting distribution of Ψ_n.

2. **Shift Correction**: This method is used to remove the higher harmonics. This method fits the unweighted distribution of the event plane, summed over all events, to a Fourier expansion, and devises an event-by-event shifting of the planes needed to make the final distribution isotropic.

3.2.7 Event Plane Resolution Correction

There is just a finite number of particles available in an event to calculate the event plane. As a result, the resolution of the measured event plane angle will be less. To calculate the actual v_2 with respect to the real reaction plane, the measured v_2 is divided by the resolution correction factor (R) [43, 31].

$$v_2 = \frac{v_2^{obs}}{R} = \frac{v_2^{obs}}{< cos[2(\Psi_2 - \Psi_R] >} \tag{3.10}$$

where Ψ_2 is the event plane angle and Ψ_R is the true reaction plane angle. The term $< cos[2(\Psi_2 - \Psi_R)] >$ is called the event plane resolution. We can express the event plane resolution as follows

$$< cos[2(\Psi_2 - \Psi_R] > = \frac{\sqrt{\pi}}{2\sqrt{2}}\chi_2 exp(-\chi_2^2/4)[I_0(\chi_2^2/4) + I_1(\chi_2^2/4)] \tag{3.11}$$

where I_x is the modified Bessel function of order and

$$\chi_2 = \frac{v_2}{\sigma} \text{ and } \sigma^2 = \frac{1}{2N}\frac{< \omega^2 >}{< \omega >^2} \tag{3.12}$$

26

where N is the total number of particles used to calculate the event plane angle and ω are the weights used to calculate the flow vector Q_n.

The ϕ-binning method is implemented to calculate the v_2 of light nuclei in Au+Au collisions at $\sqrt{s_{NN}} = 14.5$ GeV. First we obtain the raw yield of the light nuclei in various $\phi - \Psi$ bins, where ϕ is the azimuthal angle of the particle in the laboratory frame and Ψ is the event plane angle as explained in the previous subsection. Then the $\phi - \Psi$ distribution can be fitted with a function given below

$$\frac{dN}{d(\phi - \Psi)} = p_0(1 + 2p_1 cos(2(\phi - \Psi))), \tag{3.13}$$

where the fit parameter p_1 is the observed v_2 (v_2^{obs}). The v_2^{obs} is then corrected by dividing it with the proper event plane resolution correction factor to calculate the final v_2. We measure the p_T dependence of the elliptic flow can be measured by continuing the same procedure in various p_T ranges. Figure 3.6 shows the $\phi - \Psi$ distributions for d and ^3He for selected p_T ranges from minimum bias Au+Au collisions at $\sqrt{s_{NN}} = 14.5$ GeV. The $\phi - \Psi$ distributions for all p_T ranges are shown in Appendix A. The distributions are fitted with the function as given in Eq. 3.13
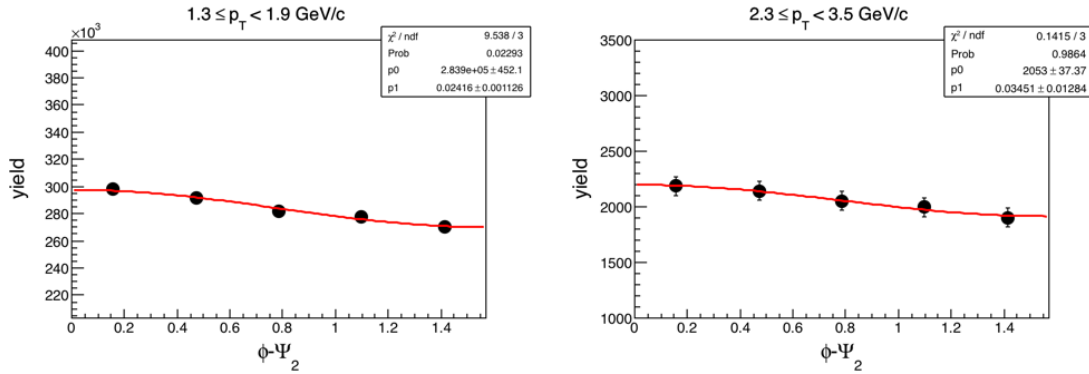
Figure 3.6: $\phi - \Psi$ distributions for d and ^3He in different p_T bins from minimum bias Au+Au collisions at $\sqrt{s_{NN}} = 14.5$ GeV. Red curves are the fit to the $\phi - \Psi$ distributions.

and the fit function is shown as red line. Then the measured v_2 is corrected for the event plane resolution [21].

Chapter 4

Results and Discussions

4.1 v_2 of light nuclei in minimum bias collisions

Figure 4.1 shows v_2 of light nuclei (d and ^3He) as a function of p_T in Au+Au collisions at $\sqrt{s_{NN}} = 14.5$ GeV for minimum bias $(0 - 80\%)$ events. The $v_2(p_T)$ of d and ^3He show a monotonically increasing trend with increasing p_T. Mass ordering of $v_2(p_T)$ i.e. lower mass particle has higher v_2 compared to heavier particles, is also observed for the light nuclei at low p_T. Such mass ordering of $v_2(p_T)$ occurs naturally in a hydrodynamic plus coalescence model of relativistic heavy-ion collisions.

Figure 4.1: v_2 as a function of p_T for d and ^3He from 0-80% of the collision centrality in Au+Au collisions at $\sqrt{s_{NN}} = 14.5$ GeV.

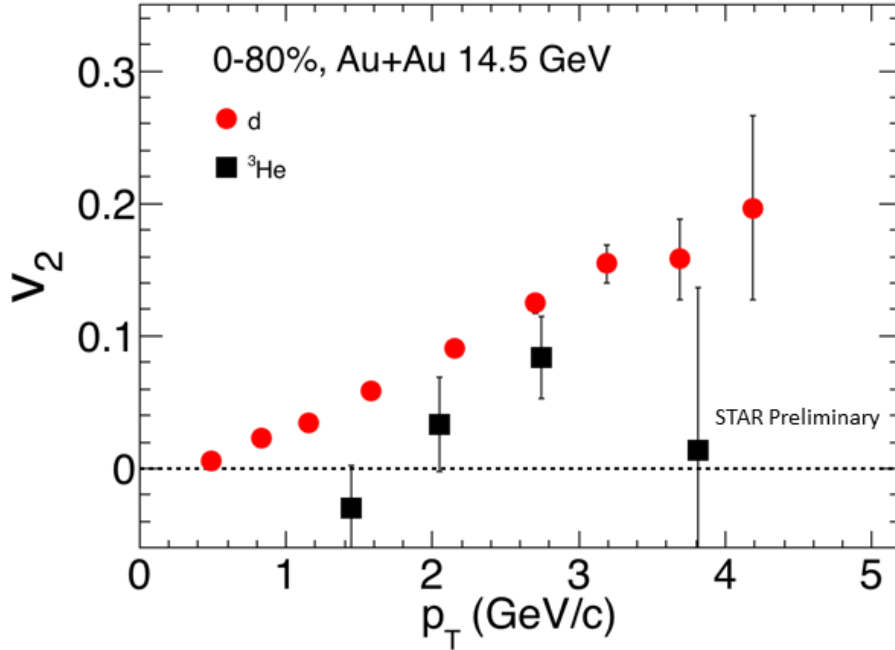The measured v_2 of light nuclei in Au+Au collisions at $\sqrt{s_{NN}} = 14.5$ GeV is also compared with the previous measurements at different collision energies ($\sqrt{s_{NN}} = 200, 62.4, 39, 27, 19.6, 11.5,$ and 7.7 GeV) as shown in Fig. 4.2 [31]. The $v_2(p_T)$ of light nuclei in Au+Au collisions at $\sqrt{s_{NN}} = 14.5$ GeV have similar trend as seen in other collision energies. The negative v_2 observed for some (anti-)nuclei at low p_T could be attributed to the interplay between transverse flow, modulation of transverse flow with respect to the reaction plane and the geometry of the source.

Figure 4.2: v_2 as a function of p_T for light nuclei from 0-80% of the collision centrality in Au+Au collisions at different collision energies.

Figure 4.3 shows the comparison of v_2 of light nuclei (d) with identified hadrons (π^+, K_s^0, and p) in Au+Au collisions at $\sqrt{s_{NN}} = 7.7$ - 200 GeV. At low $p_T (< 2$ GeV/c), mass ordering of v_2 is clearly seen for all collision energies.

4.2 Centrality dependence of light nuclei v_2

The system size dependence of v_2 of light nuclei has been studied by measuring v_2 of d in 0-30% and 30-80% centrality classes for Au+Au collisions at $\sqrt{s_{NN}} = 14.5$ GeV. Figure 4.4 shows the centrality dependence of v_2 for $d(\bar{d})$ in Au+Au collisions at different collision energies. The $v_2(p_T)$ of $d(\bar{d})$ have been measured in 0–30% and 30–80% centrality classes for Au + Au collisions at $\sqrt{s_{NN}} = 62.4$ to 7.7 GeV. But for 200 GeV, v_2 are measured in 0–10%, 10–40%, and 40–80% centrality classes. The v_2 value of light nuclei increases from central to peripheral collision. Similar centrality dependence is also observed for identified hadrons [14].
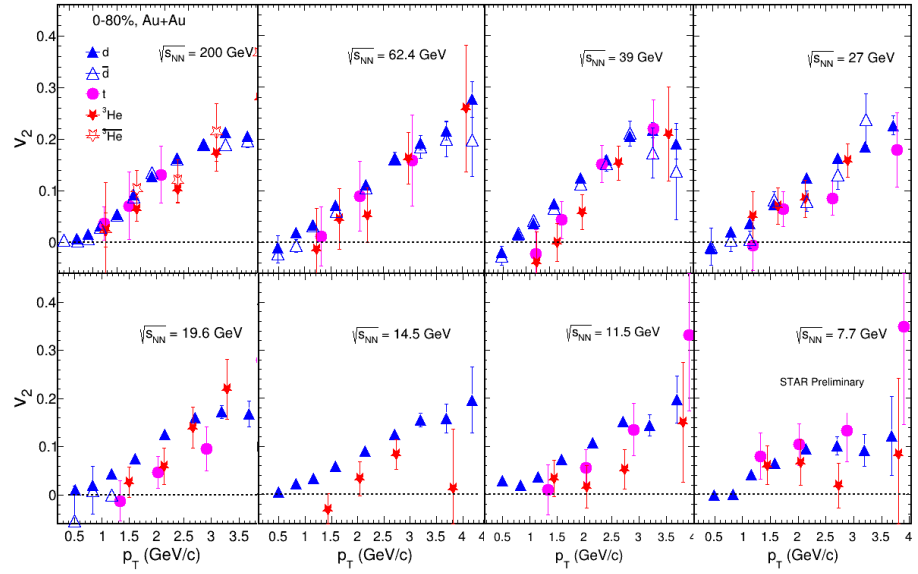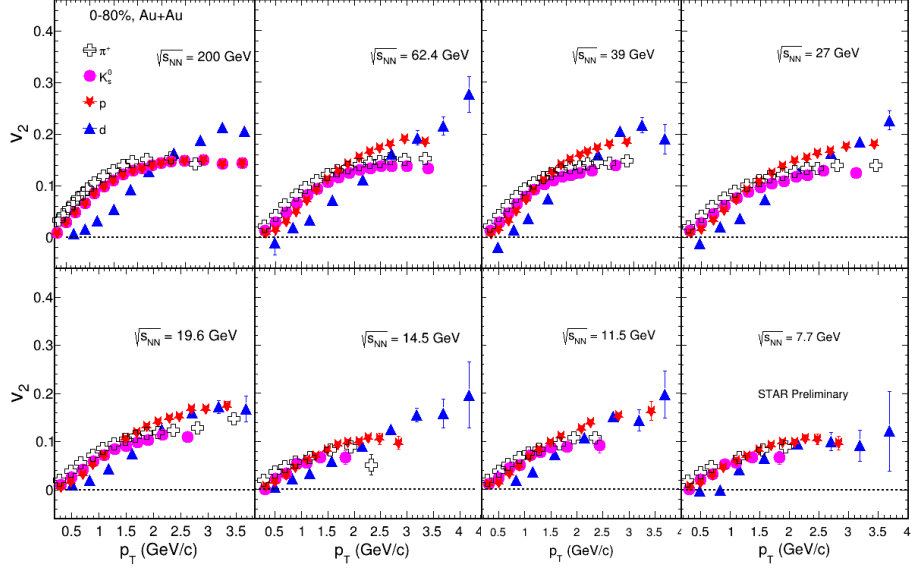
Figure 4.3: v_2 as a function of p_T for d from 0-80% of the collision centrality in Au+Au collisions at different collision energies and compared with v_2 of identified hadrons (π^+, K_s^0, and p).

4.3 Atomic mass number scaling of light nuclei v_2

Figure 4.5 shows the light nuclei v_2/A compared with the v_2 of p for that p_T/A where A is the atomic mass number of the corresponding nuclei. The motivation behind this scaling plot is to check whether the light nuclei production via the coalescence model is consistent. The dynamical coalescence model says that the light nuclei produced by the coalescence of the n nucleons, which is very close to each other in the phase space, will have $v_2(p_T)$ which is equal to n times that of the constituent nucleons. Here, $n = 2$ for d and $n = 3$ for ^3He. We observe that v_2/A of the light nuclei follows the v_2 of p for the particular p_T/A. The deviation from the simple atomic mass number scaling may be due to the more dynamic production mechanism apart from the coalescence model. However, here we can say that the relatively low production and the scaling behavior of elliptic flow followed by the light nuclei suggests the coalescence production the dominant production mechanism for light nuclei.

4.4 Dynamical Coalescence Model

Light nuclei production has been extensively studied in heavy-ion collision experiments. A popular model extensively used by the high-energy community for describing the production of light nuclei in heavy-ion collisions is the dynamical coalescence
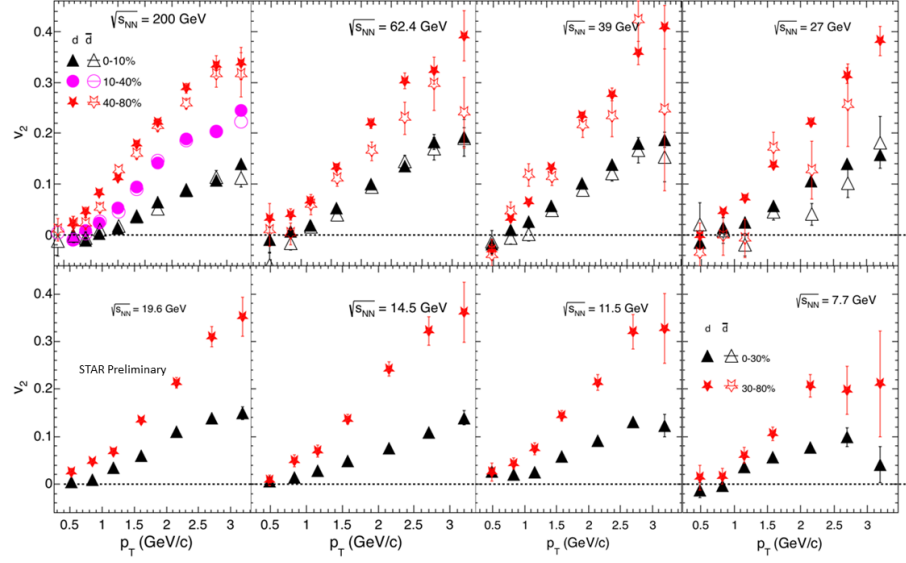
Figure 4.4: Centrality dependence of v_2 for d and $\overline{d}$ in Au+Au collisions at $\sqrt{s_{NN}} =$ 14.5 GeV and compared with other collision energies.

model. The dynamical coalescence model is incorporated in the AMPT model to calculate the deuteron production [31].

In this model, the probability of producing the light cluster of nucleons is the overlap of its Wigner phase-space density with nucleon phase-space distribution at freeze-out. For a system containing A nucleons, the momentum distribution of M-nucleon cluster with Z protons is given by [45]:

$$
\begin{aligned}
\frac{dN_M}{d^3K} = G\binom{A}{M}\binom{M}{Z}\frac{1}{A^M} \int [\prod_{i=1} Zf_p(\mathbf{r_i},\mathbf{k_i})][\prod_{i=Z+1} Mf_n(\mathbf{r_i},\mathbf{k_i})] \\
\times \rho^W(\mathbf{r_{i1}},\mathbf{k_{i1}},......,\mathbf{r_{iM-1}},\mathbf{k_{iM-1}}) \\
\times \delta(\mathbf{K}-(\mathbf{k_1}+.....+\mathbf{k_M}))d\mathbf{r_1}d\mathbf{k_1}.....d\mathbf{r_M}d\mathbf{k_M},
\end{aligned}
\tag{4.1}
$$

where f_n and f_p are the neutron and proton phase-space distribution functions at freeze-out, ρ^W is the Wigner phase-space density of M-nucleon cluster, $\mathbf{r_{i1}},......,\mathbf{r_{iM-1}}$ and $\mathbf{k_{i1}},......,\mathbf{k_{iM-1}}$ are the M-1 relative co-ordinates and momenta taken at a equal time in a M-nucleon rest frame and G is the spin-isospin statistical factor for the cluster. For the transport model simulations for heavy ion collisions the multiplicity of a M-nucleon cluster is given by

$$
N_M = G \int \sum_{i_1>i_2>....>i_M} d\mathbf{r_{i1}}d\mathbf{k_{i1}}.....d\mathbf{r_{iM-1}}d\mathbf{k_{iM-1}} < \rho_i^W(\mathbf{r_{i1}},\mathbf{k_{i1}},......,\mathbf{r_{iM-1}},\mathbf{k_{iM-1}}) >,
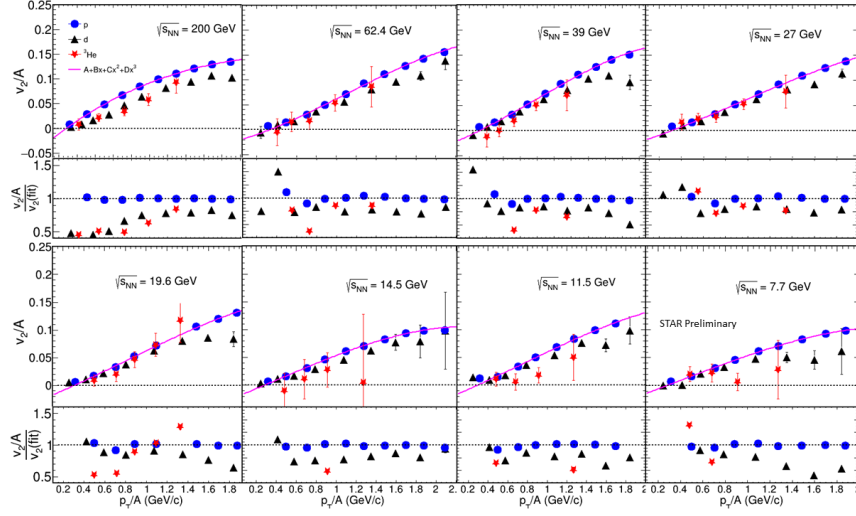$$

$$
\tag{4.2}
$$

Figure 4.5: The atomic mass number scaling of light nuclei v_2 for the various center of mass energies in Au+Au collisions. The magenta line shows the third order polynomial fit for the v_2 of p. The ratio of light nuclei v_2/A with v_2 of p for corresponding p_T/A is shown in lower panels.

where $< ... >$ denotes the event averaging, and the sum runs over all possible combinations of M nucleons containing Z protons. The isospin statistical factor G is $3/8$ for deuteron and $1/3$ for triton or ^3He, including the possibility of coalescence of deuteron with another nucleon to form triton or ^3He [45]. The coalescence model assumes that nucleon emission is statistically independent and the binding energies and quantum dynamics are not that relevant. Hence the coalescence model will be applicable if the colliding system or the emission source has the excitation energy per nucleon or temperature above ~ 9 MeV since the binding energies of the deuteron, triton, and ^3He are 2.2, 7.72 and 8.48 MeV, respectively. The coalescence model is a perturbative model and valid only if the number of clusters formed in the collision is small.

Wigner phase-space densities of d, ^3He and t

The Wigner phase-space densities for light nuclei are taken from their internal wave functions, which are considered to be same as that of spherical harmonic oscillator [45], i.e.

$$\psi(\mathbf{r_1}, \mathbf{r_2}, \mathbf{r_3}) = (3\pi^2 b^4)^{-3/4} exp(-\frac{\rho^2 + \lambda^2}{2b^2}) \tag{4.3}$$

For the above equation, the normal Jacobi co-ordinates of the three particle systems are used i.e.

$$\begin{bmatrix} \mathbf{R} \\ \boldsymbol{\rho} \\ \boldsymbol{\lambda} \end{bmatrix} = J \begin{bmatrix} \mathbf{r_1} \\ \mathbf{r_2} \\ \mathbf{r_3} \end{bmatrix} \tag{4.4}$$

where R is the center of mass coordinate, while ρ and are relative coordinates. The Jacobian matrix is given by

$$J = \begin{bmatrix} \frac{1}{3} & \frac{1}{3} & \frac{1}{3} \\ \frac{1}{\sqrt{2}} & -\frac{1}{\sqrt{2}} & 0 \\ \frac{1}{\sqrt{6}} & \frac{1}{\sqrt{6}} & -\frac{2}{\sqrt{6}} \end{bmatrix} \tag{4.5}$$

The equations 4.5 and 4.5 gives $d\mathbf{r_1}d\mathbf{r_2}d\mathbf{r_3} = 1/|J|^3 d\mathbf{R}d\boldsymbol{\rho}d\boldsymbol{\lambda}$. Here $(\mathbf{r_1} - \mathbf{R})^2 + (\mathbf{r_2} - \mathbf{R})^2 + (\mathbf{r_3} - \mathbf{R})^2 = \boldsymbol{\rho^2} + \boldsymbol{\lambda^2}$ so root mean square radius r_{rms} of triton or ^3He is

$$r_{rms}^2 = \int \frac{\rho^2 + \lambda^2}{3} |\psi(\mathbf{r_1}, \mathbf{r_2}, \mathbf{r_3})|^2 3^{3/2} d\rho d\lambda = b^2 \tag{4.6}$$

From the root mean square radii of triton and ^3He the parameter b can be determined to be 1.61 and 1.74 fm. The Wigner phase-space densities of triton and ^3He is given by

$$\rho_{t(^3He)}^W(\rho, \lambda, \mathbf{k}_\rho, \mathbf{k}_\lambda) = \int \psi(\rho + \frac{\mathbf{R_1}}{2}, \lambda + \frac{\mathbf{R_2}}{2})\psi^*(\rho - \frac{\mathbf{R_1}}{2}, \lambda - \frac{\mathbf{R_2}}{2})$$
$$\times exp(-i\mathbf{k}_\rho.\mathbf{R_1})exp(-i\mathbf{k}.\mathbf{R_2}) \tag{4.7}$$
$$= 8^2 exp(-\frac{\rho^2 + \lambda^2}{b^2})exp(-(\mathbf{k}_\rho^2 + \mathbf{k}_\lambda^2)b^2),$$

where $\mathbf{k}_\rho$ and $\mathbf{k}_\lambda$ are relative momenta which together with the total momentum K are

$$\begin{bmatrix} \mathbf{K} \\ \mathbf{k}_\rho \\ \mathbf{k}_\lambda \end{bmatrix} = J^{-,+} \begin{bmatrix} \mathbf{k}_1 \\ \mathbf{k}_2 \\ \mathbf{k}_3 \end{bmatrix} \tag{4.8}$$

with $\mathbf{k}_1, \mathbf{k}_2$ and $\mathbf{k}_3$ is the momenta of three nucleons. The matrix $J^{-,+}$ denotes the inverse of the complex conjugate transposition of the Jacobian matrix J .i.e.,

$$J^{-,+} = \begin{bmatrix} 1 & 1 & 1 \\ \frac{1}{\sqrt{2}} & -\frac{1}{\sqrt{2}} & 0 \\ \frac{1}{\sqrt{6}} & \frac{1}{\sqrt{6}} & -\frac{2}{\sqrt{6}} \end{bmatrix} \tag{4.9}$$

The Wigner phase-space densities are then given by [46]:

$$\rho^W = 8^2 exp(-\frac{\rho^2 + \lambda^2}{2b^2})exp(-(\mathbf{k}_\rho^2 + \mathbf{k}_\lambda^2)b^2), \tag{4.10}$$

where the (ρ, λ) are relative co-ordinates and the $(\mathbf{k}_\rho, \mathbf{k}_\lambda)$ are relative momentum, respectively. The b parameter is determined from the root mean square radii which is 1.96 fm for d, 1.61 fm for t and 1.74 fm for ^3He [45].

The coordinate and momentum space distributions of nucleons at freeze-out are obtained from A MultiPhase Transport (AMPT) model within the string melting scenario. The parton scattering cross-section of 3 mb has been used in the model. The data used for this project is five million Au+Au collisions at $\sqrt{s_{NN}} = 14.5$ GeV. The generated data is analyzed using ROOT (a Data analysis Framework) version 6.10.04[47].

4.4.1 AMPT model

The heavy-ion collisions at relativistic energies make the nuclear matter to be in extreme conditions of temperature and energy density, which produces a deconfined state of quarks and gluons. This deconfined state of quarks and gluons is believed to exist in the few microseconds of the universe. Many experiments were done colliding the heavy ions to study more about the properties of the so-called Quark-Gluon Plasma (QGP). They have measured many observables such as rapidity distributions of the particles and the transverse momentum spectra, the centrality dependence of these observables, and the elliptic flow of the particles. Many theoretical models were proposed to understand the extensive results obtained from the experiments. They are categorized into three :

1. Thermal models: Based on the assumption of global and thermal equilibrium.

2. Hydrodynamic models: Based on the assumption of local thermal equilibrium.

3. Transport models: Based on treating non-equilibrium dynamics explicitly.

While the thermal models explained the yield of particles and their ratios successfully, the hydrodynamic model was useful in explaining the collective behavior of low transverse momenta such as elliptic flow. The transport models treat the chemical and thermal freeze-out dynamically, they are the natural and robust tools to study more about the Hanbury-Brown-Interferometry of the hadrons. The perturbative Quantum Chromodynamics (pQCD), which uses Parton distribution functions of colliding nuclei, is used to study hard processes involving high momentum transfer. To address the evolution of Parton distribution functions at relativistic energies as well as to study the hadron rapidity distribution and its centrality dependence, the classical Yangs-Mills theory was developed. The final-state saturation model is also used to study these problems. The pQCD based studies suggest that the thermalization is achieved when we collide two very heavy nuclei at significantly high energy since the strong coupling constant is asymptotically small at saturation scale.

Nevertheless, the dense matter created in a heavy-ion collision will not achieve full thermal or chemical equilibrium since it has finite energy and volume. A Multi-Phase Model (AMPT) was developed to address the non-equilibrium many-body dynamics which incorporate initial partonic and final hadronic interactions and also the phase transition between the two phases [44].
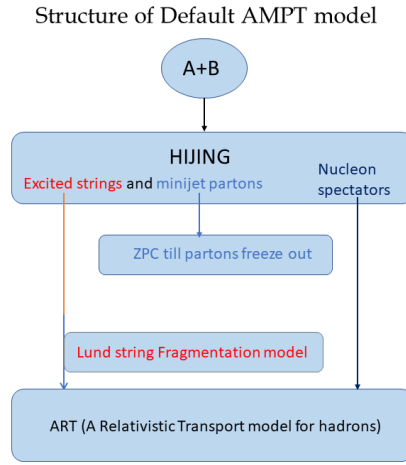
Structure of AMPT

Figure 4.6: Structure of default AMPT model.

The AMPT has four main components: initial conditions, partonic interactions, hadronization, and hadronic interactions. Each stage in AMPT uses different models as follows [44]:

1. Initial conditions: Obtained from the HIJING model, which also includes the spatial momentum distribution of mini-jet partons and soft string excitations.

2. Partonic interactions: Partonic scattering is described using Zhang's Parton Cascade (ZPC), which includes two-body scattering cross-section obtained from pQCD with screening masses.

3. Hadronization: The conversion of partons to hadrons is based on the Lund string fragmentation model or by the quark coalescence model.

4. Hadronic Interactions: The dynamics of the resulting hadrons are based on the hadronic cascade described by A Relativistic Transport (ART) model.

Types of AMPT - Default and String Melting

Based on the two models used in the third stage of the AMPT i.e., the hadronization stage AMPT is classified into two variants.
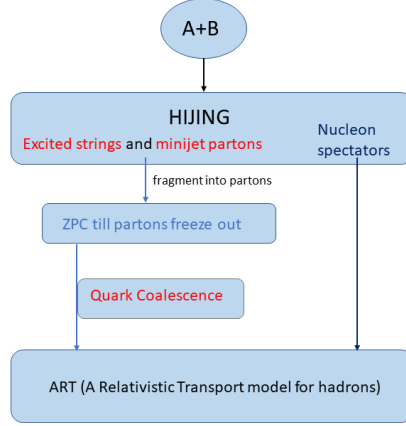
Structure of string melting AMPT model

Figure 4.7: Structure of string melting AMPT model.

1. Default AMPT model: In this model, when the partons stop interacting, they are combined with their parent strings and converted to hadrons using the Lund string fragmentation model (Figure 4.6).

2. String Melting AMPT model (AMPT-SM): In the AMPT model with string melting, the quark coalescence model is used to describe the conversion of partons to hadrons (Figure 4.7)

4.5 Data Analysis using AMPT model

The data set used in the analysis is generated using the String Melting Scenario in AMPT model for Au+Au collisions at $\sqrt{s_{NN}} = 14.5$ GeV. The data was generated for 5 million events, and the Lund String Fragmentation parameters a = 0.55 and b = 0.15 is used. The output text files contain the information about particle ID, mass, position coordinates, and the momentum coordinates. The root file is generated encapsulating all the information from the text files arranged in the branches of the tree. These root files are used for further analysis. As a preliminary check for data, some basic Quality Assurance (QA) plots are obtained. Then using the charged particle multiplicity distribution at the mid-rapidity ($|\eta| < 0.5$), the centrality cuts of 0-10%, 10-20%, 20-40%, 40-60% and 60 -80% are determined as shown in the Figure 4.8.

The left panel of Fig. 4.9 shows the transverse momentum (p_T) spectra of deuteron for different centrality classes in Au+Au collisions at $\sqrt{s_{NN}} = 14.5$ GeV. The right panel of Fig. 4.8 shows comparison of p_T spectra of deuteron with the experimental
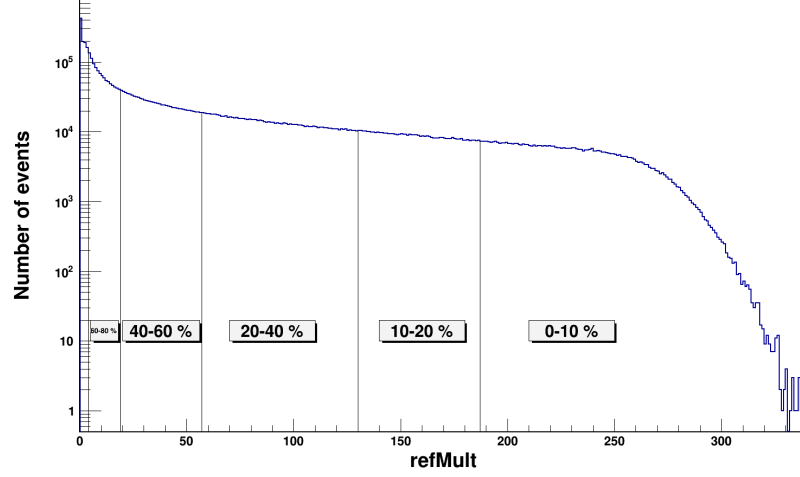
Figure 4.8: Reference multiplicity distribution with indication of different centrality classes in Au+Au collisions at $\sqrt{s_{NN}} = 14.5$ GeV from AMPT model.

data [48]. It shows that the AMPT model underestimates the experimental data.

The left panel of Fig. 4.10 shows the elliptic flow of $d + \bar{d}$ for 0-30% and 30-80% centrality classes in Au+Au collisions at $\sqrt{s_{NN}} = 14.5$ GeV. The v_2 of deuteron increases as a function of p_T. The v_2 is higher for 30-80% centrality compared to 0-30% centrality. The right panel of Fig. 4.9 shows the comparison of v_2 of deuteron with the experimental data. It shows that the AMPT model significantly deviates from the experimental data for peripheral collisions. It qualitatively describes the v_2 of deuteron for the central collisions.
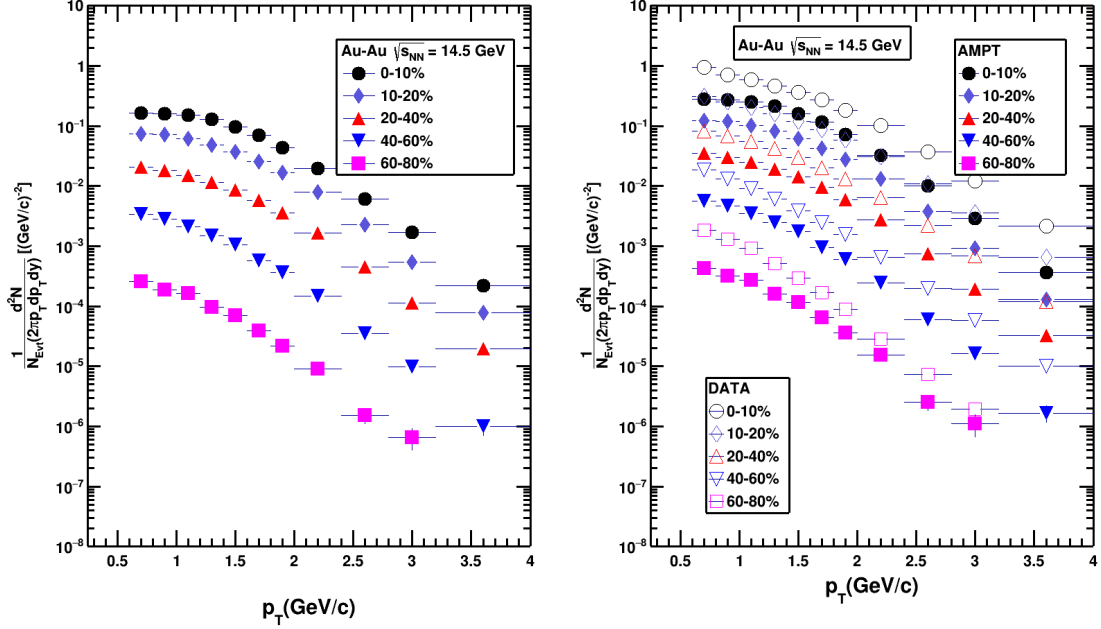
Figure 4.9: Transverse momentum spectra for d (left panel) and the comparison with the data (right panel) in Au+Au collisions at $\sqrt{s_{NN}} = 14.5$ GeV from AMPT model for different centralities.
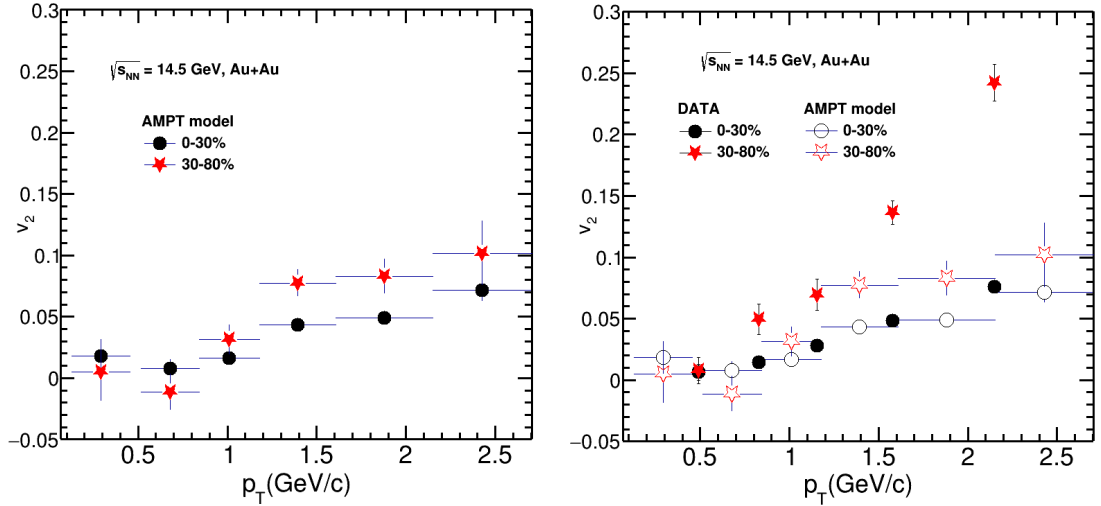

Figure 4.10: Elliptic Flow for d (left panel) and the comparison with the data (right panel) in Au+Au collisions at $\sqrt{s_{NN}} = 14.5$ GeV from AMPT model for different centralities.

Chapter 5

Conclusion

In this thesis, we present the measurements of elliptic flow of light nuclei in Au+Au collisions at $\sqrt{s_{NN}} = 14.5$ GeV using the event plane method. This data were recorded by the STAR experiment in the years 2014 as a part of first phase of the Beam Energy Scan Program at RHIC. The main detectors used in this analysis are Time Projection Chamber and Time of Flight. The transverse momentum dependence of elliptic flow of light nuclei in Au+Au collisions at $\sqrt{s_{NN}} = 14.5$ GeV is presented. The v_2 of light nuclei increases with increasing p_T in the measured p_T range. The light nuclei v_2 exhibits mass ordering at low p_T suggesting the role of strong radial flow in the medium. The negative v_2 observed at low p_T is consistent with the presence of strong radial flow as it is supposed to push low p_T particles to high p_T region.

The centrality dependence of v_2 for light nuclei has been studied in Au+Au collisions at $\sqrt{s_{NN}} = 14.5$ GeV and compared with other collision energies. The $v_2(p_T)$ of light nuclei decreases from peripheral to central collision which is consistent with centrality dependence of v_2 for identified hadrons. The higher v_2 in peripheral collision is attributed to the initial elliptic collision geometry.

The atomic mass number scaling for the elliptic flow of the light nuclei has been studied for $\sqrt{s_{NN}} = 14.5$ GeV, and compared with other center of mass energies. It shows that the elliptic flow of light nuclei for all collision energies follow the atomic mass number scaling, which confirms that the coalescence model describes the light nuclei production in relativistic heavy-ion collisions reasonably well. Nevertheless, some deviations suggest that there are more dynamical processes involving in the light nuclei production.

A model-based study is performed using transport+coalescence model to find the theoretical prediction of light nuclei v_2 in Au+Au collisions at $\sqrt{s_{NN}} = 14.5$ GeV. In this model, the probability for producing a light nucleus cluster is determined by the overlap of its Wigner phase-space density and the nucleon phase-space distribution at

freeze-out. The coordinate and momentum space distributions of nucleons at freeze-out are taken from A MultiPhase Transport model within the string melting scenario. The model failed to describe the p_T spectra and v_2 of light nuclei in all measured p_T ranges and centrality classes. The model seems to describe the v_2 of light nuclei for the central collisions but significantly deviates from the data for peripheral collisions. Further optimization of model parameters are required to better describe the data.

A more systematic and differential study of p_T-spectra and v_2 of light nuclei can shed light on the production mechanism of light nuclei in relativistic heavy-ion collisions.

Appendix A

Z distributions and (ϕ - Ψ_2) distributions for d and ^3He in Au+Au collisions at $\sqrt{s_{NN}}$= 14.5 GeV for 0-80% centrality.

The Z-distributions of light nuclei for various p_T bins are shown below. For each p_T bin, there are five ($\phi - \Psi_2$) bins i.e., $0 - \frac{\pi}{10}$, $\frac{\pi}{10} - \frac{2\pi}{10}$, $\frac{2\pi}{10} - \frac{3\pi}{10}$, $\frac{3\pi}{10} - \frac{4\pi}{10}$ and $\frac{4\pi}{10} - \frac{5\pi}{10}$. The same method is used to extract the yields for other p_T bins.
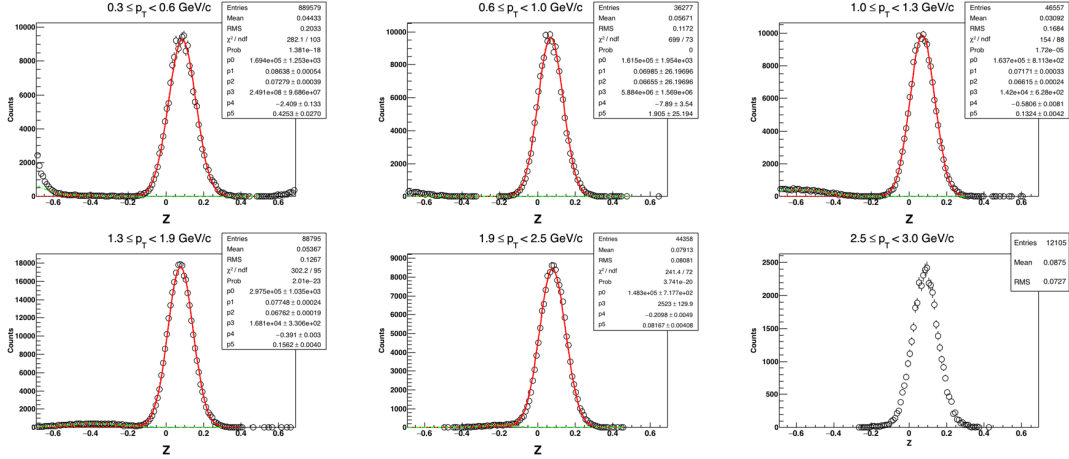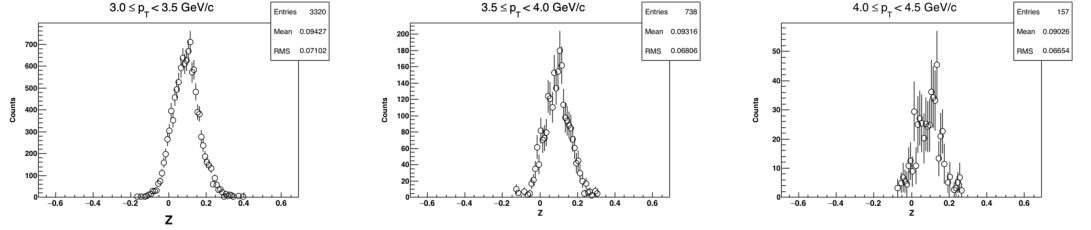
Figure A.1: Z-distribution of d of $0 < (\phi$ - $\Psi_2) < \pi/10$ in Au+Au collisions at $\sqrt{s_{NN}}=$ 14.5 GeV for various p_T bins. The Z distribution is fitted with two gaussian where the one gaussian (red solid line) shows the nuclei of interest and the other gaussian (green dashed line) is used to describe background.

Figure A.2: Z-distribution of ^3He of $0 < (\phi$ - $\Psi_2) < \pi/10$ in Au+Au collisions at $\sqrt{s_{NN}}=$ 14.5 GeV for various p_T bins. The Z distribution is fitted with two gaussian where the one gaussian (red solid line) shows the nuclei of interest and the other gaussian (green dashed line) is used to describe background.
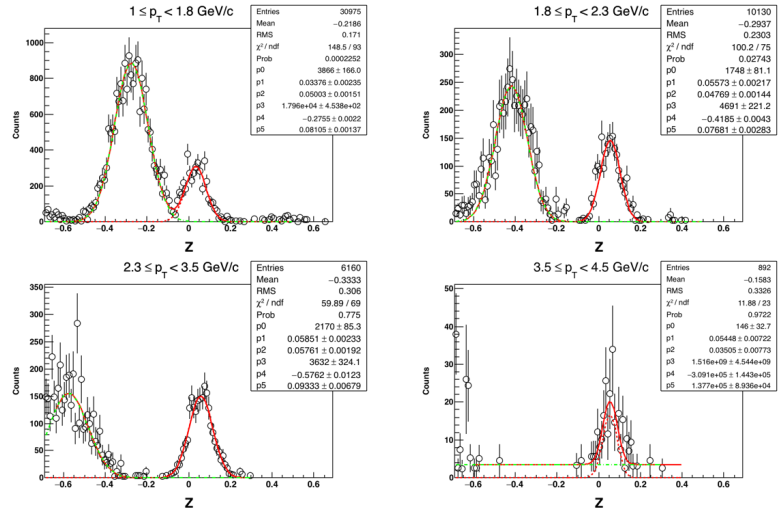
Figure A.3: ($\phi - \Psi_2$) distribution of d for various p_T bins in minimum bias Au+Au collisions at $\sqrt{s_{NN}}$= 14.5 GeV. The solid red line shows the fit to the distribution.
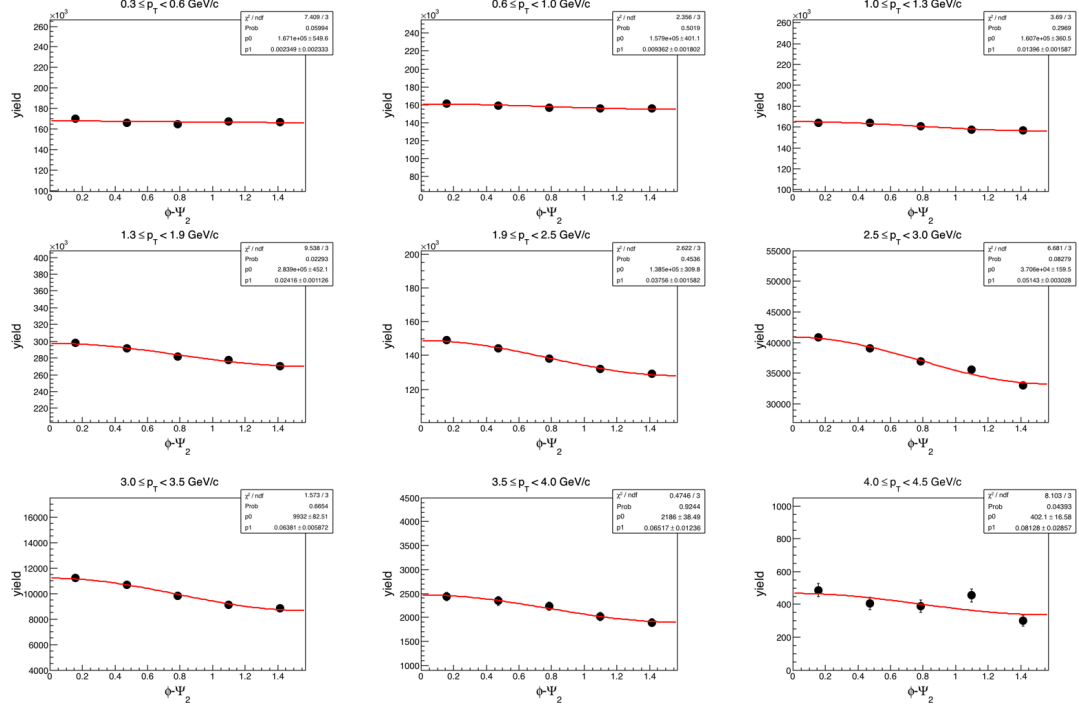

Figure A.4: ($\phi - \Psi_2$) distribution of ^3He for various p_T bins in minimum bias Au+Au collisions at $\sqrt{s_{NN}}$= 14.5 GeV. The solid red line shows the fit to the distribution.
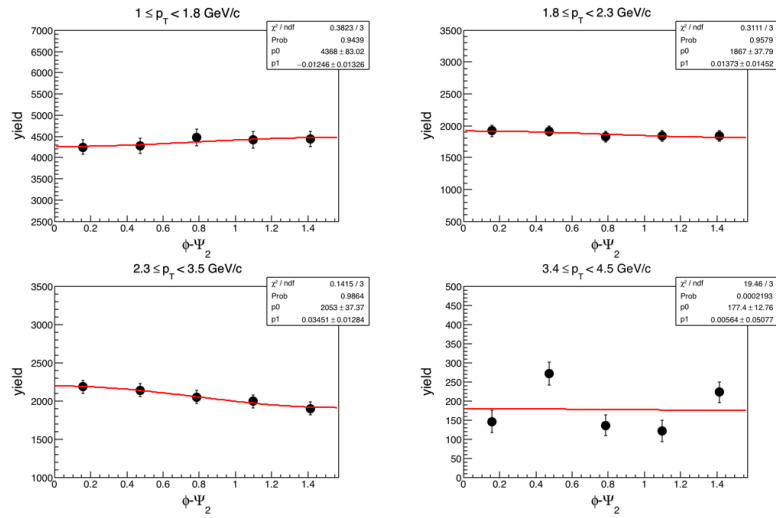
Bibliography

[1] D. J. Gross and F. Wilczek, Phys. Rev. Lett. 30, 1343 (1973).

[2] H. Politzer, Phys. Rev. Lett. 30, 1346 (1973).

[3] S. Bethke, Prog. Part. Nucl. Phys. 58, 351 (2007).

[4] J. C. Collins and M. J. Perry, Phys. Rev. Lett. 34, 1353 (1975).

[5] F. Karsch, Nucl. Phys. A 698, 199 (2002).

[6] S. Gupta et al. Science 332, 1525 (2011).

[7] B. I. Abelev et al. (STAR Collaboration), Phys. Rev. C 79, 034909 (2009).

[8] A. K. Aamodt et al. (ALICE Collaboration), Phys. Rev. Lett. 105, 072002 (2010).

[9] Barbara Betz, arXiv:0910.4114 (2009).

[10] Pasechnik, R. and Šumbera, M., Universe, 3, 7 (2017).

[11] https://drupal.star.bnl.gov/STAR/files/ChitrasenJenaThesis.pdf.

[12] J. L. Nagle et al., Phys. Rev. C53, 367-376 (1996).

[13] L. Adamczyk et al., Phys. Rev. C94, 034908 (2016).

[14] L. Adamczyk et al. (STAR Collaboration), Phys. Rev. C 88, 014902 (2013).

[15] L. P. Csernai and J. I. Kapusta, Phys. Rep. 131, 223 (1986).

[16] A. Z. Mekjian, Phys. Rev. C 17, 1051 (1978).

[17] H.H. Gutbrod et al., Phys. Rev. Lett. 37, 667 (1976).

[18] S. Das Gupta and A.Z. Mekjian, Phys. Rep. 72, 131 (1981).

[19] J.-Y. Ollitrault, Phys. Rev. D 46, 229 (1992).

[20] R. Snellings, New Journal of Physics, 13 (2011).

[21] S. Voloshin and Y. Zhang, Z. Phys. C 70, 665 (1996).

[22] D. Molnar and S. A. Voloshin, Phys. Rev. Lett. 91, 092301 (2003)

[23] C. Adler et al. (STAR Collaboration), Phys. Rev. C 66, 034904 (2002).

[24] J. Adams et al. (STAR Collaboration), Phys. Rev. C 72, 014904 (2005).

[25] Satoshi Ozaki and Thomas Roser, Prog. Theor. Exp. Phys., 3, 03A102 (2015).

[26] V. H. Ranjbar, S. Y. Lee, L. Ahrens, M. Bai, K. Brown,W. Glenn, H. Huang, A. Luccio, W. W. MacKay,V. Ptitsyn, T. Roser, and N. Tsoupas, Phys. Rev., 051001 (2004).

[27] https://www.star.bnl.gov/central/experiment/.

[28] http://www.bnl.gov/rhic/.

[29] K. H. Ackermann et al. (STAR Collaboration), Nucl. Instr. Meth. A 499, 624 (2003).

[30] K. Adcox et al. (PHENIX Collaboration), Nucl. Instr. Meth. A 499, 469 (2003).

[31] M. Adamczyk et al. (BRAHMS Collaboration), Nucl. Instr. Meth. A499, 437 (2003).

[32] B. B. Back et al. (PHOBOS Collaboration), Nucl. Inst. Meth. A 499, 603 (2003).

[33] M. Anderson et al., Nucl. Instr. Meth. A 499, 659 (2003).

[34] K. H. Ackermann et al., Nucl. Instr. Meth. A 499, 713 (2003).

[35] B. Bonner et al., Nucl. Instr. Meth. A 508, 181 (2003).

[36] M. Beddo et al., Nucl. Instrum. Meth. A 499, 725 (2003).

[37] C. E. Allgower et al., Nucl. Instrum. Meth. A 499, 740 (2003).

[38] M. M. Aggarwal et al., Nucl. Instr. Meth. A 499, 751 (2003).

[39] H. Wieman et al., IEEE Trans. Nuc. Sci. 44, 671 (1997); J. Thomas et al., Nucl. Instum Meth. A 478, 166 (2002).

[40] D. Liko, STAR Note 00087, 1–15 (1992).

[41] H. Bichsel, Nucl. Instr. Meth. A 562 154 (2006).

[42] W. M. Yao et al., J. Phys. G: Nucl. Part. Phys. 33, 1 (2006).

[43] S. Voloshin, A. M. Poskanzer, Phys.Rev. C 58, 1671-1678 (1998).

[44] Z.-W. Lin et al., Phys. Rev. C72, 064901 (2005).

[45] L.-W. Chen et al., Nucl. Phys. A729, 809–834 (2003).

[46] S. Gupta et al., Phys. Rep. 72, 1981; R. Scheibl et al., Phys. Rev. C59, 1999.

[47] R. Brun and F. Rademakers, Nucl. Instrum. Meth., A389, 81–86 (1997).

[48] J. Adam et al., Phys.Rev. C 99, 064905 (2019).